Monthly Notices of the ROYAL ASTRONOMICAL SOCIETY

MNRAS **524,** 5524–5547 (2023) https://doi.org/10.1093/mnras/stad2134
Advance Access publication 2023 July 31

MUSE–ALMA Haloes – IX. Morphologies and stellar properties of gas-rich galaxies

Arjun Karki,[1★] Varsha P. Kulkarni,[1★] Simon Weng,[2,3,4,5] Céline Péroux,[2,6] Ramona Augustin,[7] Matthew Hayes,[8] Mohammadreza Ayromlou,[9] Glenn G. Kacprzak,[5,10] J. Christopher Howk,[11] Roland Szakacs,[2] Anne Klitsch,[12] Aleksandra Hamanowicz,[7] Alejandra Fresco,[13] Martin A. Zwaan,[2] Andrew D. Biggs,[2] Andrew J. Fox,[14] Susan Kassin[7] and Harald Kuntschner[2]

[1]*Department of Physics and Astronomy, University of South Carolina, Columbia, SC 29208, USA*
[2]*European Southern Observatory, Karl-Schwarzschildstrasse 2, D-85748 Garching bei München, Germany*
[3]*Sydney Institute for Astronomy, School of Physics, University of Sydney, Sydney, NSW 2006, Australia*
[4]*ARC Centre of Excellence for All Sky Astrophysics in 3 Dimensions (ASTRO 3D), Canberra, Australian Capital Territory 2611, Australia*
[5]*ATNF, CSIRO Astronomy and Space Science, PO Box 76, Epping, NSW 1710, Australia*
[6]*CNRS, LAM (Laboratoire d'Astrophysique de Marseille), Aix Marseille Université, UMR 7326, F-13388 Marseille, France*
[7]*Space Telescope Science Institute, 3700 San Martin Drive, Baltimore, MD21218, USA*
[8]*Department of Astronomy and Oskar Klein Centre for Cosmoparticle Physics, AlbaNova University Centre, Stockholm University, SE-10691, Stockholm, Sweden*
[9]*Institut für theoretische Astrophysik, Universität Heidelberg, Zentrum für Astronomie, Albert-Ueberle-Str 2, D-69120 Heidelberg, Germany*
[10]*Centre for Astrophysics and Supercomputing, Swinburne University of Technology, Hawthorn, Victoria 3122, Australia*
[11]*Department of Physics, University of Notre Dame, Notre Dame, IN 46556, USA*
[12]*DARK, Niels Bohr Institute, University of Copenhagen, Jagtvej 128, DK-2200 Copenhagen, Denmark*
[13]*Max-Planck-Institut für Extraterrestrische Physik (MPE), Giessenbachstrasse 1, D-85748 Garching, Germany*
[14]*AURA for ESA, Space Telescope Science Institute, 3700 San Martin Drive, Baltimore, MD 21218, USA*

Accepted 2023 July 12. Received 2023 July 11; in original form 2022 December 30

ABSTRACT

Understanding how galaxies interact with the circumgalactic medium (CGM) requires determining how galaxies' morphological and stellar properties correlate with their CGM properties. We report an analysis of 66 well-imaged galaxies detected in *Hubble Space Telescope* and Very Large Telescope MUSE observations and determined to be within ± 500 km s^{-1} of the redshifts of strong intervening quasar absorbers at $0.2 \lesssim z \lesssim 1.4$ with H I column densities $N_{\rm HI} > 10^{18}$ cm^{-2}. We present the geometrical properties (Sérsic indices, effective radii, axis ratios, and position angles) of these galaxies determined using GALFIT. Using these properties along with star formation rates (SFRs, estimated using the Hα or [O II] luminosity) and stellar masses (M_* estimated from spectral energy distribution fits), we examine correlations among various stellar and CGM properties. Our main findings are as follows: (1) SFR correlates well with M_*, and most absorption-selected galaxies are consistent with the star formation main sequence of the global population. (2) More massive absorber counterparts are more centrally concentrated and are larger in size. (3) Galaxy sizes and normalized impact parameters correlate negatively with $N_{\rm HI}$, consistent with higher $N_{\rm HI}$ absorption arising in smaller galaxies, and closer to galaxy centres. (4) Absorption and emission metallicities correlate with M_* and specific SFR, implying metal-poor absorbers arise in galaxies with low past star formation and faster current gas consumption rates. (5) SFR surface densities of absorption-selected galaxies are higher than predicted by the Kennicutt–Schmidt relation for local galaxies, suggesting a higher star formation efficiency in the absorption-selected galaxies.

Key words: galaxies: evolution – *(galaxies:)* quasars: absorption lines – galaxies: stellar content – galaxies: structure.

1 INTRODUCTION

The circumgalactic medium (CGM) has become increasingly recognized as an important component of the baryonic Universe. It serves as a transition region between the galaxy disc and the intergalactic medium (IGM) (Tumlinson, Peeples & Werk 2017). Metal-poor IGM gas is believed to flow into the galaxy, passing through the CGM. This gas is converted into stars and progressively enriched chemically. The outflows driven by the supernovae (or active galactic nuclei) transfer the enriched gas back into the IGM, also passing through the CGM. This cosmic baryon cycle regulates star formation in the galaxy (Péroux & Howk 2020). Given the central role of the CGM in this cycle, it is expected to play a major role in the evolution of the galaxy. Understanding how the CGM interacts with galaxies requires analysing how the stellar properties of the galaxies are dictated by and, in return, influence the CGM properties.

★ E-mail: karkia@email.sc.edu (AK); kulkarni@sc.edu (VPK)

The stellar properties of galaxies are described by measurements of various properties that depend directly on their stellar populations – for example, photometric magnitudes, colours, star formation rates (SFRs), and stellar masses. The morphologies of the galaxies are closely coupled to these properties. They can be expressed in terms of various quantitative measures of the surface brightness distribution such as the effective radius (R_e), axis ratio (b/a), and Sérsic index (n). Broadly speaking, galaxies fall into two main types in the colour–magnitude diagrams – the 'blue cloud' consisting of the late-type, more actively star-forming galaxies (SFGs), and the 'red sequence' of early-type, more passive galaxies that have their star formation quenched (e.g. Kauffmann et al. 2003; Buta 2013).

The 'size' of a galaxy detected in optical light depends on its stellar mass and the rate of star formation, which are governed by the dark matter halo and the galaxy's formation history. Massive galaxies are larger and have higher SFRs (Mowla et al. 2019). The slope of the size versus stellar mass relation is shallower for late-type galaxies than for early-type galaxies (e.g. Shen et al. 2003; van der Wel et al. 2014). This difference may be due to dry minor mergers, which can lead to a size growth caused by adding an outer envelope without adding as much mass. Galaxies that undergo repeated dry minor mergers tend to have a larger size (e.g. Carollo et al. 2013; Hilz, Naab & Ostriker 2013). The star formation caused by gas-rich mergers can also lead to the formation of larger discs. The different evolutionary paths taken by early-type and late-type galaxies thus result in different size–mass relationships.

The direct observation of emissions from the gas inflows and outflows passing through the CGM is difficult due to the very low gas density. Absorption spectroscopy of background sources such as quasars or gamma-ray bursts (GRBs) provides an alternative and powerful technique to study these gas flows. Damped Ly α (DLA) and sub-Damped Ly α (sub-DLA) systems provide a huge reservoir of neutral hydrogen required for star formation (e.g. Péroux et al. 2003; Wolfe, Gawiser & Prochaska 2005; Prochaska & Wolfe 2009; Noterdaeme et al. 2012; Kulkarni et al. 2022). DLAs ($N_{\rm HI} \geq 2 \times 10^{20}\,{\rm cm}^{-2}$) and sub-DLAs ($10^{19} \leq N_{\rm HI} < 2 \times 10^{20}\,{\rm cm}^{-2}$) permit measurements of a variety of metal ions, and are therefore among the best-known tracers of element abundances in distant galaxies (e.g. Kulkarni et al. 2005; Rafelski et al. 2012; Som et al. 2015; Fumagalli, O'Meara & Prochaska 2016).

Although the absorption technique provides an effective tool to probe gas along the sight line to the background object, it cannot provide information about the galaxy in which the absorption arises (e.g. Bergeron 1986; Bergeron & Boissé 1991). Also, detecting galaxies associated with absorbers in the vicinity of the quasar using imaging and spectroscopy was not always effective in past studies, since the galaxies selected for spectroscopic study were sometimes found to be offset in redshift from the absorber. The technique of integral field spectroscopy (IFS) provides an efficient method for detecting galaxies associated with the absorbers, and thus connecting stellar properties with gas properties (Péroux et al. 2019, 2022). Several surveys [e.g. MusE GAs FLOw and Wind (MEGAFLOW; Schroetter et al. 2016), MUSE Ultra Deep Field (MUDF; Fossati et al. 2019), and MUSE Analysis of Gas around Galaxies (MAGG; Dutta et al. 2020; Lofthouse et al. 2020, 2023)] have used the power of IFS to search for sources traced by Mg II and H I absorption and studied the gas properties of CGM. While the Bimodal Absorption System Imaging Campaign (BASIC survey; Berg et al. 2023) has studied H I selected partial Lyman limit systems (pLLSs) and Lyman limit systems (LLSs) to search for absorber-associated galaxies, the Cosmic Ultraviolet Baryon Survey (CUBS; Chen et al. 2020) has studied the galactic environments of LLSs at $z_{\rm abs} < 1$ using IFS observations. Another survey, MUSE Quasar-field Blind Emitters Survey (MUSEQuBES; Muzahid et al. 2020), searched for Ly α emitters at the redshift of the absorbers using guaranteed time observations with the Multi-Unit Spectroscopic Explorer (MUSE; Bacon et al. 2010) on the Very Large Telescope (VLT).

We have surveyed a large number of absorption-selected galaxies with VLT MUSE and the Atacama Large Millimetre/submillimetre Array (ALMA; Wootten & Thompson 2009) as part of our MUSE–ALMA Haloes (MAH) Survey, and have recently imaged these galaxies with the *Hubble Space Telescope (HST)*. The *HST* images provide high-resolution broad-band continuum imaging of the galaxies, while the MUSE data provide IFS of the galaxies, thus providing information about the spatial distribution of gas kinematics, SFRs, and emission-line metallicity. The kinematics measured from the IFS also allows estimates of the dynamical masses of the galaxies (e.g. Péroux et al. 2012; Bouché et al. 2013). Thus, combining *HST* images and MUSE IFS provides a powerful approach to studying the morphologies and stellar content of absorption-selected galaxies and relating them to the CGM gas properties. Together, the stellar and gas properties can be used to put improved constraints on the evolution of galaxies and their CGM.

The MAH survey targets the fields of 32 H I rich absorbers at redshift $0.2 \leq z_{\rm abs} \leq 1.4$ detected in sight lines to 19 quasars. These 32 absorbers were detected in HST FOS, COS, or STIS UV spectra. Most of our quasars also have optical high-resolution spectra from VLT/UVES, X-Shooter, or Keck/HIRES with spectral resolutions ranging from 4000–18 000 (X-shooter), 45 000–48 000 (HIRES), and up to 80 000 (UVES). The H I column densities determined from these UV spectra (with resolution $R = 20\,000$–$30\,000$) are found to be $N_{\rm HI} > 10^{18}\,{\rm cm}^{-2}$. Information about quasar spectra and an overview of the survey are provided in Péroux et al. (2022). In this paper, we focus on 66 galaxies observed in the *HST* images that lie within a radial velocity range of ± 500 km s^{-1} of the redshifts of 25 H I rich absorbers (the remaining seven absorbers having no associated galaxies within ± 500 km s^{-1}). The paper is organized as follows: Section 2 presents the sample selection and observations. Section 3 details the results derived from the observation. Section 4 summarizes our findings. We adopt the following cosmology parameters: $\rm H_o = 70\,km\,s^{-1}\,Mpc^{-1}$, $\Omega_M = 0.3$, and $\Omega_\Lambda = 0.7$ throughout the paper.

2 HST IMAGES AND OBSERVATIONS

Our primary *HST* imaging data set comes from the broad-band imaging observations performed in GO Program ID 15 939 (PI: Péroux) with the Wide Field Camera-3 (WFC3). These data were complemented by archival Wide Field and Planetary Camera-2 (WFPC2) or WFC3 images obtained in programs 5098, 5143, 5351, 6557, 7329, 7451, 9173, and 14 594 (PIs Burbidge, Macchetto, Bergeron, Steidel, Malkan, Smette, Bechtold, Bielby, respectively). The observations consisted of multiple dithered exposures in a variety of filters. Further details about these observations and the observation strategy used for our own program (PID 15939) can be found in Péroux et al. (2022).

The data were reduced using the CALWF3 or CALWF2 pipelines. For each filter, the sky-subtracted, aligned images from the individual exposures were median-combined to produce the final images. Figs 1 and 2 show examples of final full-frame images and zoomed-in sections near the quasar. The quasar point spread function (PSF) has been subtracted in the zoomed-in frame to search for galaxies at small angular separations from the quasar. The PSF in each filter and instrument for each given quasar field was constructed using observations of all remaining quasar fields from our sample in the

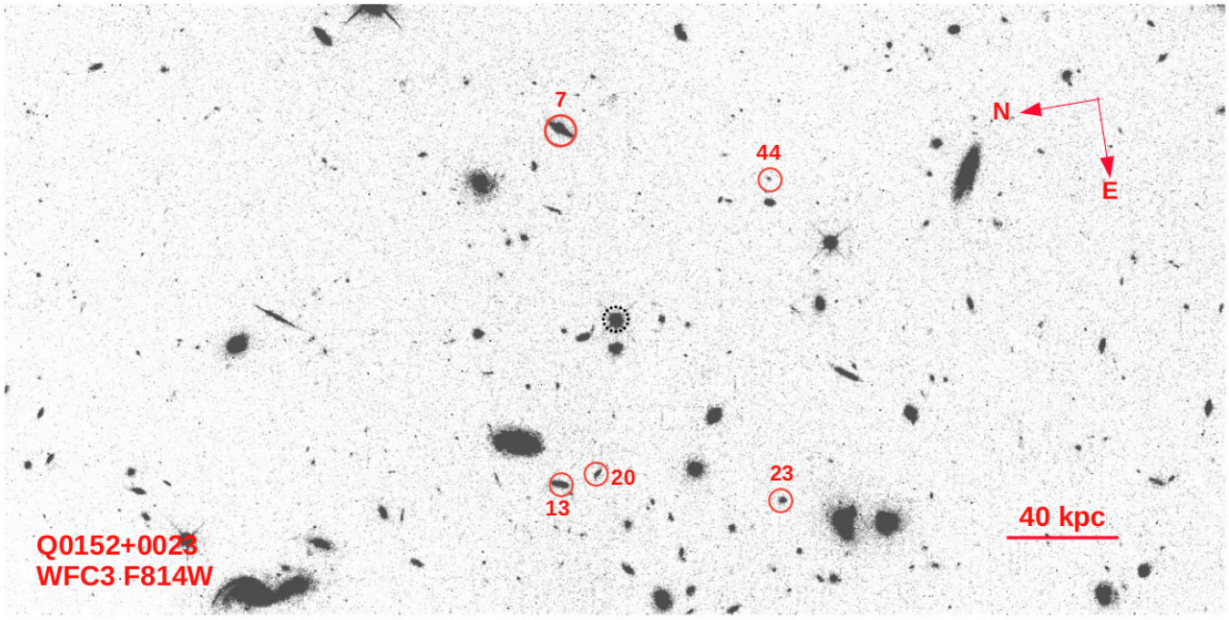

Figure 1. Median-stacked HST WFC3 image of the field of Q0152+0023 in the *F*814*W* UVIS filter. The image is created by combining all the individual exposure images, which helps to remove the cosmic ray effects and bad pixels and improve the signal-to-noise ratio. This enables us to study the morphological properties of the galaxy populations robustly. The solid red circles represent the positions of the absorber-associated galaxies in the field of view, while the dotted black circle denotes the QSO's position. The ASTROPY PHOTUTILS package was used to detect the associated galaxies in the given quasar field. The redshifts of the associated galaxies (determined from our MUSE data) are within ± 500 km $^{s^{-1}}$ of the absorber redshift. The scale bar shown corresponds to 40 kpc at $z_{\rm abs} = 0.4818$. The object identification numbers (IDs) of these galaxies are the same as in the MAH master table listed in Péroux et al. (2022).

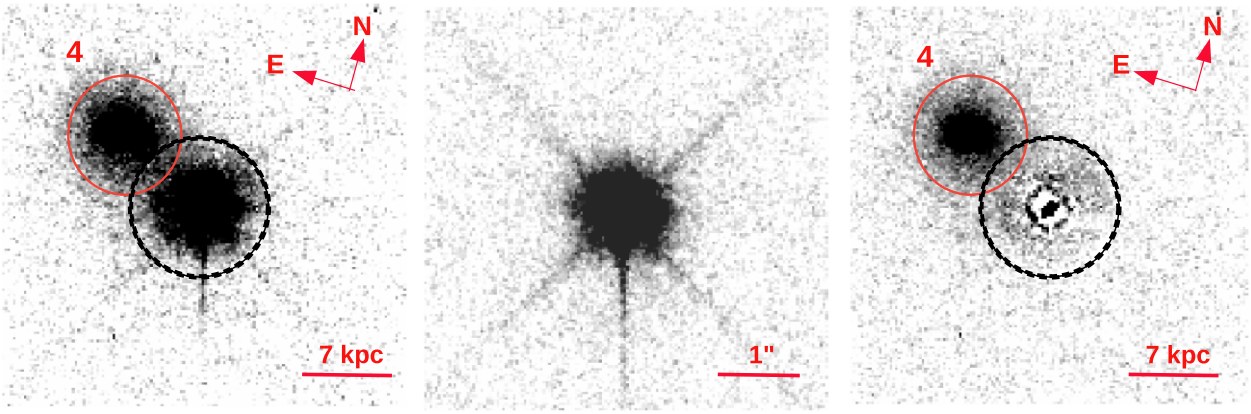

Figure 2. Left panel: Median-stacked zoomed-in image for Q1515+0410 in the *F*814*W* UVIS filter-band. The image shows the bright background quasar (exhibiting strong diffraction spikes) with a foreground galaxy. The dotted black and solid red circles denote the location of the quasar and the galaxy in the image. The quasar's light contaminates the galaxy's image. Middle panel: A PSF constructed to remove quasar contamination. The PSF is designed using observations of all other quasar fields from our sample in the same filter. Right panel: PSF-subtracted image of the same zoomed-in image. The contamination from the quasar is removed after performing a careful PSF subtraction. Detailed information about PSF construction and PSF subtraction is provided in Péroux et al. (2022).

same band and instrument. For each such image used in making the PSF, we masked the objects other than the central quasar and performed sky subtraction. All such processed images were aligned spatially and coadded after the flux levels in the outer wings of the PSF were scaled to match with each other. The resulting PSF thus constructed was subtracted from the quasar field of interest after matching the flux levels of the two images. The PSF-subtracted images thus produced were used to search for galaxies near the quasars. This approach is similar to that used in previous works (e.g. Kulkarni et al. 2000, 2001; Chun et al. 2010; Straka, Kulkarni & York 2011; Augustin et al. 2018). Object detections and astrometric and photometric measurements were performed using the ASTROPY package PHOTUTILS. The data reduction, PSF construction, PSF subtraction, and photometric measurements are further detailed in Péroux et al. (2022). Figs A1−A6 in Appendix A show the full-frame images of the remaining quasar fields.

Using the MUSE observations along with the *HST* imaging, a total of 3658 sources were detected in all of our fields. The MUSE Line Emission Tracker (MUSELET) tool of the MPDAF package was used to detect sources with emission lines, and the PROFOUND

Table 1. Summary of HST observations. Listed are the quasar name, quasar and absorber redshifts, the full width at half-maximum of the PSF of *HST* image in each filter, the field of view, the *HST* camera and filter used, the number of exposures and exposure time of each exposure, and the 3σ limiting magnitude in each filter. A complete table of quasar fields and their properties is available as machine-readable online material.

Quasar	z_{qso}	z_{abs}	FWHM (arcsec)	FOV (arcsec × arcsec)	Instrument	$n_{exp} \times t_{exp}$ [s]	Magnitude limit
Q0058+0019	1.959	0.6127	0.188	80 × 80	WFPC2/WF3 *F*702*W*	4 × 1100	27.02
Q0138−0005	1.340	0.7821	0.073	160 × 80	WFC3/UVIS F475W	4 × 567	28.70
–	–	–	0.083	160 × 80	WFC3/UVIS *F*625*W*	4 × 591	28.90
–	–	–	0.130	123 × 123	WFC3/IR *F*105*W*	4 × 603	27.93
J0152−2001	2.060	0.3897	0.083	160 × 80	WFC3/UVIS *F*336*W*	2 × 587 + 2 × 595	29.39
–	–	0.7802	0.074	160 × 80	WFC3/UVIS *F*475*W*	2 × 587 + 2 × 595	29.29
–	–	–	0.182	80 × 80	WFPC2/WF3 *F*702*W*	2 × 1100 + 3 × 1300 + 1 × 1400	27.68
Q0152+0023	0.589	0.4818	0.083	160 × 80	WFC3/UVIS *F*336*W*	2 × 535 + 2 × 518	28.54
–	–	–	0.074	160 × 80	WFC3/UVIS *F*475*W*	1 × 635 + 3 × 618	28.39
–	–	–	0.082	160 × 80	WFC3/UVIS *F*814*W*	1 × 635 + 3 × 618	27.92
–	–	–	–	–	–	–	–

R Package was used to identify continuum sources in the MUSE fields. A final master table was produced by matching the sources detected in the HST images with the MUSE results using the TOPCAT tool. Spectroscopic redshifts were determined for 703 objects out of the 3658 sources detected in all fields using the MARZ tool on the VLT/MUSE spectra. The remaining objects do not have spectroscopic redshifts, because they were either detected outside of the MUSE field of view or too faint to estimate a redshift. We refer the reader to Péroux et al. (2022) for a detailed methodology regarding the redshift measurements and for the master table of all targets.

Table 1 provides a summary of *HST* imaging observations for 18 quasar fields. The high spatial resolution of the broad-band *HST* images allowed us to detect several sources nearby or far away from the quasar sightlines, which were undetected in the MUSE cubes. The *HST* images also enabled us to detect and resolve several sources near the quasars whose redshifts are not well known. While the MUSE data allowed us to study the emission properties of galaxies, the study of geometrical properties of the galaxies and structural features such as tidal tails are difficult to discern in MUSE images due to insufficient spatial resolution. The high-resolution *HST* images also allowed us to study the morphologies of the galaxies and structural details.

The MUSE data show 79 associated galaxies within ±500 km s^{-1} of the absorber redshifts. Out of the total of 32 absorbers, 19 (59 per cent) have two or more associated galaxies, seven (22 per cent) have one associated galaxy, and the remaining six (19 per cent) have no associated galaxy detected within ±500 km s^{-1} of the absorption redshift. A detailed explanation of how these associated galaxies were selected is provided in Weng et al. (2023). Out of these 79 galaxies, nine galaxies were detected in emission only in MUSE fields (but not in *HST* images), one galaxy was detected at the edge of the *HST* image, and three galaxies were detected in the archival *HST* images but were too faint to perform reliable morphological measurements. Therefore, we analysed the remaining 66 associated galaxies in the 18 *HST* fields.

3 ANALYSIS AND RESULTS

3.1 Morphological properties of associated galaxies

The GALAPAGOS software (Häußler et al. 2011) was used to study the morphologies of the 66 galaxies associated with the absorbers in our MAH sample. GALAPAGOS uses SEXTRACTOR (Bertin & Arnouts 1996) for object detection and GALFIT (Peng et al. 2002) for two-dimensional image decomposition, and can be run in batch mode to analyse multiple objects. This GALAPAGOS analysis was performed on the reddest images obtained for each quasar field because these images in the red or near-infrared filters (WFPC2 *F*702*W*, *F*814*W*, WFC3 *F*105*W*, WFC3 *F*140*W*, or NICMOS *F*160*W*) provide far more sensitive detection thresholds and enable better deblending of extended sources compared to the bluer filters. The redder bands better sample the cooler and older stars, which in turn more accurately follow the gravitational potential.

Sérsic profiles were fitted to each of the sample galaxies. In each case, a cut-out region was created with the galaxy centred in the image. Depending on the size of the galaxy, the cut-out region ranged from 3 arcsec × 3 arcsec to 7 arcsec × 7 arcsec in size, and included a sufficient number of pixels at the sky level surrounding the source. Most of the cut-out images show only the galaxy without the presence of nearby sources. In cases where nearby sources were present, they were masked using the segmentation map made using SEXTRACTOR. For each object, the best-fitting values of the morphological parameters were determined so as to minimize the residual between the data and the fitted Sérsic model. In cases where there were significant residuals or the parameter values returned by GALAPAGOS had large errors, the morphological parameters were determined by adding more Sérsic components and individually running GALFIT iteratively until the parameter converged. As an example, Fig. 3 shows the outcomes of the Sérsic profile fitting for the five associated galaxies detected in the UVIS/*F*814*W* image of the quasar field presented in the Fig. 1. Each of these five galaxies were well-fitted using a single Sérsic component.

Table 2 lists the morphological parameters [R_e, n, b/a, and PA of the major axis (in degrees east of north)] along with impact parameter, k-corrected absolute magnitude, absolute effective surface brightness, and reduced chi-squared values determined from our analysis for each of the galaxies using *HST* images. The galaxy redshifts are based on the emission line measurements from our MUSE observations, as described in Péroux et al. (2022). The absolute magnitude for each galaxy was determined using the apparent magnitude and luminosity distance for the assumed cosmological parameters and k-corrected.

Since our sample consists of galaxies at different redshifts observed in various bandpasses, applying a k-correction is essential to make a meaningful comparison among them (Blanton & Roweis 2007). The IDL-based software KCORRECT was used to calculate k-corrections to the absolute magnitudes. Fig. 4 shows the distribution of the morphological properties provided by GALFIT and the galaxies redshift of the associated galaxies. For our sample galaxies, the Sérsic index ranges from 0.33 to 2.27 with a median value of

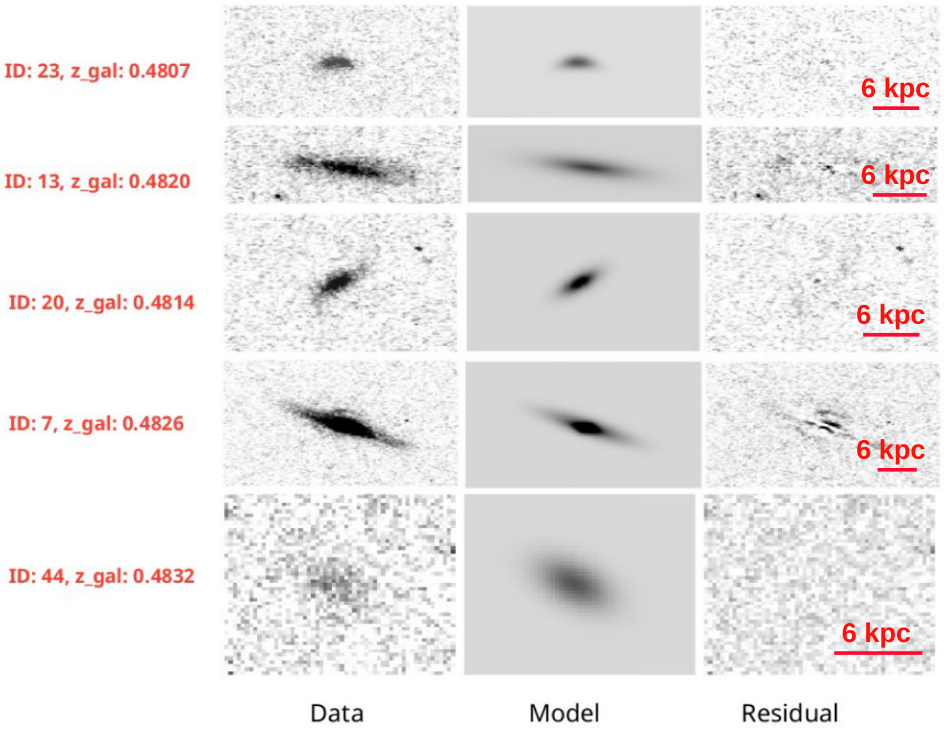

Figure 3. Results of the Sérsic profile fitting using GALFIT for the absorber-associated galaxies presented in Fig. 1. The panels show galaxy images in UVIS/*F*814*W* band (left panels), the best-fitting Sérsic model (middle panels), and the residual images (right panels). The orientation of the images is the same as in Fig. 1.

Table 2. Results of our GALFIT morphological modelling, impact parameters (b), and surface brightness of the gas-rich galaxies. The listed parameters are the quasar name, object IDs from Péroux et al. (2022), impact parameters of the quasar sightlines from the galaxy centres, *k*-corrected absolute magnitude in the UVIS *F*814*W* filter, Sérsic index, effective radius, axis ratio, position angle (PA) of the major axis, absolute surface brightness averaged within the effective radii of the galaxies, and the goodness of fit. A complete table of associated galaxies and their properties is available as machine-readable online material.

Object	ID	b [kpc]	Absolute mag [*F*814*W*]	*n*	R_e [kpc]	*b/a*	PA [deg.]	$<\mu_{\rm eff}>$ [mag arcsec^{-2}]	χ^2_ν
Q0138 − 0005	14	79.7	-21.39 ± 0.02	0.84 ± 0.01	1.92 ± 0.02	0.70 ± 0.01	106.38 ± 0.74	18.59 ± 0.03	1.093
Q0152 − 2001	13	83.8	-20.60 ± 0.07	1.88 ± 0.08	6.12 ± 0.34	0.57 ± 0.01	136.06 ± 1.66	21.90 ± 0.14	1.127
Q0152 − 2001	4	170	-22.29 ± 0.01	1.53 ± 0.02	5.01 ± 0.06	0.30 ± 0.00	140.92 ± 0.22	19.77 ± 0.03	1.365
Q0152 − 2001	5	60.7	-21.46 ± 0.04	1.24 ± 0.03	6.55 ± 0.16	0.32 ± 0.00	154.40 ± 0.37	21.19 ± 0.07	1.136
–	–	–	–	–	–	–	–	–	–

0.86 ± 0.07. This suggests that most of the sample galaxies are discs or dwarf spheroidals. Such disc galaxies exhibit an exponential light profile (Kelvin et al. 2012). The effective radii of the sample galaxies range from 0.68 to 7.55 kpc with a median value of 2.85 ± 0.15 kpc, and their absolute magnitudes (in *F*814*W* filter) range from −15.80 to −23.73 with a median value of -20.81 ± 0.07. The redshifts of the galaxies range from $z = 0.19$ to $z = 1.15$, with a median value $z = 0.56$.

3.2 Stellar properties of associated galaxies

The SFRs of the associated galaxies were measured using the Hα emission line for the sample galaxies with $z \leq 0.4$, and with [O II] emission lines for the remaining galaxies (where the Hα emission lines fall outside the MUSE wavelength coverage). Dust-corrected SFRs were calculated for 13 galaxies at redshift $z < 0.4$ with detections of Hα and Hβ using the measured Hβ and Hα emission-line fluxes. For 15 galaxies, only a 3σ upper limit could be placed on the SFR. A complete description of the SFR estimates and dust correction on SFRs is provided by Weng et al. (2023). The stellar masses (M_*), estimated using the *HST* broad-band magnitudes and performing spectral energy distribution (SED) fits using the photometric redshift code LE PHARE (Arnouts et al. 1999; Ilbert et al. 2006), were found to span a wide range $7.8 < \log M_* < 12.4$. Further detail about the stellar mass determination is provided in Augustin et al. (in preparation).

The SFR surface density and average stellar mass density within the effective radius were calculated as

$$\Sigma_{\rm SFR} = \frac{\rm SFR}{2\pi {\rm R_e^2}} \quad (1)$$

$$\Sigma_{\rm M_*} = \frac{M*}{2\pi {\rm R_e^2}} \quad (2)$$

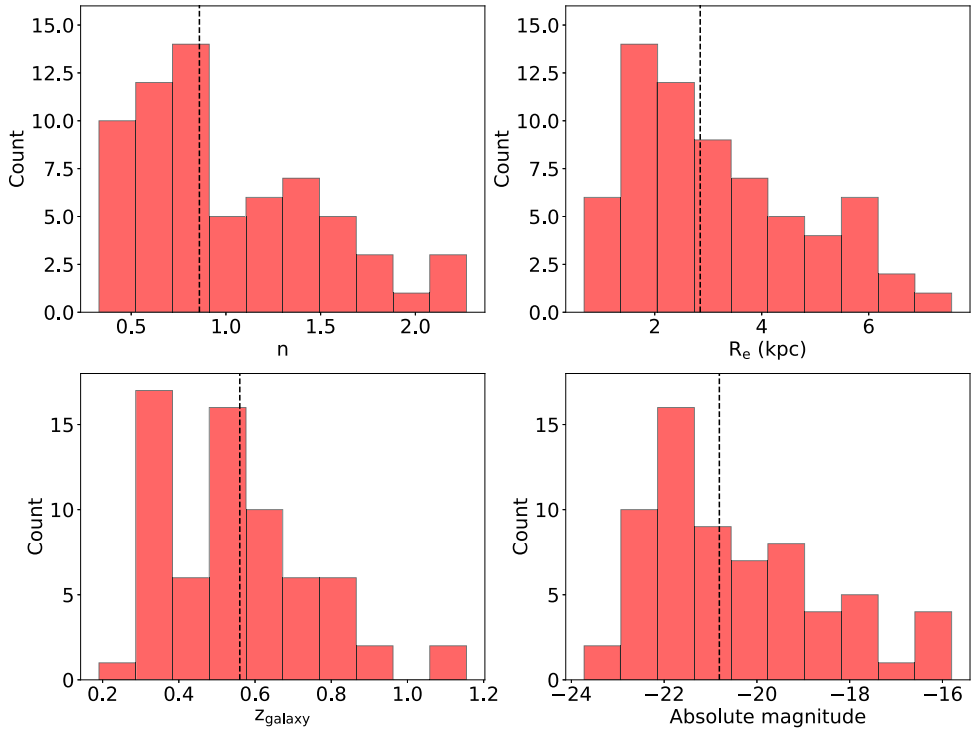

Figure 4. The frequency distribution of the Sérsic index (upper left), effective radius (upper right), galaxy's redshift (lower left), and the *k*-corrected absolute magnitude (lower right) in UVIS/*F*814*W* filter of the 66 absorber-associated galaxies. In each panel, the vertical dashed black line represents the median value.

The absolute effective surface brightness, $<\mu_{\rm eff}>$ (mag arcsec^{-2}), averaged within the effective radius for our galaxies were calculated based on the k-corrected absolute magnitude and the effective radius using the following expression (Graham & Driver 2005):

$$< \mu_{\rm eff} >= {\rm M} + 5\log_{10}({\rm R_e}) + 38.57 \quad (3)$$

Table 3 lists the derived stellar properties of the galaxy populations.

3.3 Absorption properties of associated galaxies

The MAH survey analysed the absorption properties of 32 H I rich absorbers with $N_{\rm HI} > 10^{18}$ cm^{-2} using 19 quasar fields. Using the *HST* images of the 18 quasar fields, we detected 66 galaxies within $\pm$ 500 km s^{-1} of the absorber redshift for 25 absorbers. Table 4 lists the impact parameters of the quasar sightlines from the galaxy centres and the absorption properties along these sightlines for the sample galaxies and the galaxies from the literature. The impact parameters of these 66 associated galaxies are measured from the astrometry of the *HST* images. The measurements of the column density of H I, absorption metallicities, and the equivalent widths of the Fe II λ 2600 and Mg II λ 2796 absorption lines are from various references in the literature.

The absorption metallicities listed for the DLAs and sub-DLAs in the sample (available for four out of the 25 absorbers) are based on the Zn abundance without corrections for ionization and (in most cases) dust depletion. The effect of dust depletion is expected to be modest, since Zn is a volatile element that is far less depleted in the interstellar medium (ISM) of the Milky Way compared to refractory elements such as Fe (e.g. Jenkins 2009; Vladilo et al. 2011). Indeed, Zn is often used as the metallicity indicator in DLA/sub-DLAs for these reasons. Ionization corrections are known to be small for DLAs (Muzahid et al. 2016; Péroux & Howk 2020). For sub-DLAs (which tend to be more ionized than DLAs), the ionization corrections for Zn abundance are found to be $\lesssim$0.2 dex (e.g. Meiring et al. 2009). We therefore select only the absorbers with Zn abundance measurements for comparison of the absorption metallicities with the stellar properties of the galaxies in the following sections. Finally, we note that emission-line metallicities are also available for our galaxies, and were measured using the R_3 calibration from Curti et al. (2017). A complete description of the galaxy metallicity estimates is provided in Weng et al. (2023).

4 DISCUSSION

Using the high-resolution *HST* images and the IFS provided by MUSE, we have studied and analysed the morphological and stellar properties of 66 associated galaxies. The softwares GALAPAGOS and LE PHARE provide detailed information about the structural and stellar properties of these gas-rich galaxies. The following sections discuss the scientific results, compare the associated galaxies with the general galaxy population, and explore the connection between their stellar and absorption properties.

4.1 Literature sample

To examine how the properties of the galaxies in our sample compare to other absorption-selected galaxies, we use a comparison sample compiled from the literature. Specifically, this literature sample consists of 61 galaxies detected at the redshifts of known gas-rich absorbers from the IFS surveys of the CGM (see references listed in Table 4). These literature galaxies range in redshift from 0.10 to 3.15, and in impact parameter from $\sim$3 to 88 kpc. The H I column density of some of the literature galaxies (Zabl et al. 2019, denoted as grey stars in the figures) are estimated from the Mg II λ2796 equivalent widths using the relation from Ménard & Chelouche (2009). Three absorbers from this literature sample have multiple galaxies at the

Table 3. Stellar properties of the gas-rich galaxies and other galaxies from the literature. The listed parameters are the quasar name, galaxy ID, galaxy's redshift, specific star formation rate, SFR surface density, stellar mass surface density, and sSFR surface density. The entries marked '−999' correspond to measurements that are unavailable. A complete table of associated galaxies and their properties is available as machine-readable online material.

Object	ID	z_{gal}	Log sSFR [yr^{-1}]	Log Σ_{SFR} [$M_\odot yr^{-1}$ kpc^{-2}]	Log Σ_{M*} [$M_\odot kpc^{-2}$]	Log Σ_{sSFR} [yr^{-1} kpc^{-2}]
Q0138−0005	14	0.7821	-8.96 ± 0.21	-0.53 ± 0.15	8.44 ± 0.15	-10.33 ± 0.21
Q0152−2001	13	0.3814	-11.46 ± 0.62	-3.33 ± 0.58	8.13 ± 0.22	-13.83 ± 0.62
Q0152−2001	4	0.3814	−999	−999	9.33 ± 0.08	−999
Q0152−2001	5	0.3826	-10.92 ± 0.17	-2.10 ± 0.10	8.82 ± 0.14	-13.35 ± 0.17
–	–	–	–	–	–	–

Note. The SFRs and $M*$ for our sample galaxies are from Weng et al. (2023) and Augustin et al. (in preparation), respectively. The SFR and $M*$ for the literature sample are from Augustin et al. (2018), Rhodin et al. (2021), Christensen et al. (2014), Zabl et al. (2019), Lundgren et al. (2012), and Ma et al. (2018).

Table 4. Absorption properties of the gas-rich galaxies and other absorbers from the literature. Listed are the name of the quasar field, absorber redshift, impact parameter of the nearest galaxy, normalized impact parameter (b/R_e), H I column density, rest equivalent widths of Mg II λ2796 and Fe II λ2600, the absorption metallicities, the element used as the metallicity indicator, and the references. The absorption metallicities listed here are the observed values (based generally on Zn) in the quasar sightlines. The last column lists the references for the impact parameter, absorber rest-frame equivalent widths, absorption metallicity, and the H I column density. See the text for more details. The entries marked '−999' correspond to measurements that are unavailable. A complete table of absorption properties is available as machine-readable online material.

Object	$z_{abs.}$	b [kpc]	b/R_e	log N_{HI} [cm^{-2}]	W_r Mg II 2796 [Å]	W_r Fe II 2600 [Å]	$[X/H]_{abs}$	X	References
Q0138−0005	0.7821	79.70	41.50 ± 0.22	19.81 ± 0.08	1.21 ± 0.10	1.10 ± 0.11	0.28 ± 0.16	Zn	[1, 4, 21, 30]
Q0152−2001	0.7802	54.30	9.28 ± 0.27	18.87 ± 0.12	0.36 ± 0.04	<0.30	−999	−999	[1, 30]
*Q*0152−2001	0.3830	60.70	9.26 ± 0.22	<18.80	0.58 ± 0.05	−999	−999	−999	[1, 5, 30]
Q0152+0023	0.4818	120.90	62.64 ± 2.31	19.78 ± 0.08	1.34 ± 0.06	0.88 ± 0.06	−999	−999	[1, 30]
–	–	–	–	–	–	–	–	–	–

Note. References: [1] This work [2] Hamanowicz et al. (2020), [3] Boisse et al. (1998), [4] Péroux et al. (2008), [5] Rahmani et al. (2018), [6] Prochaska et al. (2007), [7] Fynbo et al. (2011), [8] Bashir et al. (2019), [9] Krogager et al. (2017), [10] Hartoog et al. (2015), [11] Zafar et al. (2017), [12] Bouché et al. (2012), [13] Berg et al. (2016), [14] Wolfe et al. (2008), [15] Kashikawa et al. (2014), [16] Christensen et al. (2014), [17] Augustin et al. (2018), [18] Rhodin et al. (2021), [19] Péroux et al. (2011), [20] Péroux et al. (2019), [21] Péroux et al. (2008), [22] Rhodin et al. (2018), [23] Boisse et al. (1998), [24] Rahmani et al. (2016), [25] Péroux et al. (2016), [26] Wolfe & Wills (1977), [27] Kacprzak et al. (2011), [28] Berg et al. (2017), [29] Churchill (2001), [30] Rao, Turnshek & Nestor (2006), [31] Meiring et al. (2007), [32] Ledoux et al. (2006), [33] Ma et al. (2018), [34] Lundgren et al. (2012), [35] Zabl et al. (2019)

absorber redshifts (Augustin et al. 2018). In these cases, if combined measurements of stellar properties were available, we adopted those values and treated those multiple sources as a single source. The stellar masses for the galaxies in the literature sample were derived from SED fitting in most cases, and using the tight correlation between M_* and a dynamical estimator, i.e. a function of galaxy velocity dispersion and rotational velocity (Schroetter et al. 2019) in a few cases. The SFRs were measured using H α, Ly α, or [O II] emission line fluxes. The emission metallicities for the literature sample are from Christensen et al. (2014), Augustin et al. (2018), and Rhodin et al. (2018).

4.2 Correlations between stellar and absorption properties

To assess the correlations between the various properties of the galaxies associated with the absorbers, we use the Spearman rank-order correlation method to evaluate the correlation coefficient (r_s) and the probability (p) that the observed value of r_s could occur purely by chance. In cases where there is a mixture of detections and limits (i.e. in the presence of censored data), we use the survival analysis method to calculate the Spearman correlation coefficient [as implemented in the IMAGE REDUCTION AND ANALYSIS FACILITY (IRAF; Tody 1986) task SPEARMAN]. The survival analysis method uses the Kaplan–Meier estimate of the survival curve to assign ranks to the observations that include censored points. Censored points are assigned half (for upper limits) or twice (for lower limits) the rank that they would have had were they uncensored.

Given that the literature sample is based on observations obtained with different selection methods, it is useful to ask how much the correlations are affected by the inclusion or exclusion of the literature sample. With this in mind, we computed the r_s and p values between the various properties for both our own sample, and a larger sample after including the literature galaxies. Table 5 lists the results of these correlation calculations. In the following subsections, we discuss some of the key implications of our analysis to address two major questions: How do absorber-selected galaxies compare to the general galaxy population? How do stellar and absorption properties relate?

4.3 Do gas-rich galaxies differ from the general population?

We now compare the absorber-associated galaxies from our sample and the literature with the properties of the overall galaxy population. While making these comparisons, we examine whether there is a difference between galaxies associated with high and low H I column densities, and also between small versus large impact parameters. The galaxies with the lowest impact parameters may be thought of as the host galaxies of the absorbers (e.g. Schroetter et al. 2016; Weng et al. 2023). In most cases (18 out of 24), the galaxies with the lowest impact parameters are also the most massive galaxies.

4.3.1 Dependence of μ_{eff} on luminosity

Fig. 5 shows the absolute effective rest-frame surface brightness against absolute magnitude relation, where the galaxies are colour-coded by the H I column density of the absorber associated with

Table 5. Results of correlation tests between various properties of our sample galaxies and literature galaxies. Column 1 lists the parameter pairs for which the correlation is computed. Columns 2, 3, and 4 list the number of paired parameters, the Spearman rank order correlation coefficient (r_s), and the probability (p) that the observed value of r_s could arise by chance, for both the sample galaxies and the literature galaxies. Columns 5, 6, and 7 list similar values for our sample galaxies only. The last column lists the figure and the panel number showing the corresponding data, where the first index denotes the figure number, and the second and third indices denote the column number (from left to right) and row number (top to bottom) of the panel in the figure.

Parameters	$N_{\rm total}$	$r_{\rm s,\,total}$	$p_{\rm total}$	$N_{\rm sample}$	$r_{\rm s,\,sample}$	$p_{\rm sample}$	Figure panel
M_{F814W}, $<\mu_{\rm eff}>$	79	0.761	4.19×10^{-16}	66	0.734	2.17×10^{-12}	5, 1, 1
log M_*, log SFR	88	0.411	1.24×10^{-4}	60	0.404	2.19×10^{-3}	6, 1, 1
log M_*, $R_{\rm e}$	97	0.492	9.77×10^{-7}	60	0.578	1.33×10^{-6}	7, 1, 1
log M_*, n	75	0.430	2.51×10^{-4}	60	0.474	1.31×10^{-4}	7, 2, 1
R_e, b	97	0.259	1.05×10^{-2}	66	0.096	4.44×10^{-1}	8, 1, 1
log M_*, W_r (Mg II 2796 Å)	51	−0.272	4.86×10^{-2}	60	−0.397	1.68×10^{-3}	9, 1, 1
log M_*, $[X/H]_{\rm emi}$	70	0.434	5.68×10^{-3}	35	0.330	8.10×10^{-2}	10, 2, 1
log sSFR, $[X/H]_{\rm emi}$	70	−0.401	2.07×10^{-2}	35	−0.246	2.37×10^{-1}	10, 2, 3
log SFR, $[X/H]_{\rm emi}$	70	−0.012	9.42×10^{-1}	35	0.170	3.88×10^{-1}	10, 2, 2
log $N_{\rm HI}$, b/R_e	45	−0.556	2.00×10^{-4}	31	−0.393	3.14×10^{-2}	12, 1, 1
log $N_{\rm HI}$, R_e	45	−0.517	6.00×10^{-4}	31	−0.326	7.45×10^{-2}	12, 2, 1
log $N_{\rm HI}$, log $\Sigma_{\rm sSFR}$	41	0.418	8.30×10^{-3}	22	0.121	5.23×10^{-1}	13, 1, 2
log $N_{\rm HI}$, log $\Sigma_{\rm SFR}$	42	0.287	6.65×10^{-2}	23	−0.215	3.14×10^{-1}	13, 1, 1
b/R_e, $[X/H]_{\rm abs}$	20	0.433	5.12×10^{-2}	5			11, 2, 1
b, $[X/H]_{\rm abs}$	28	0.423	2.80×10^{-2}	5			11, 1, 1
log M_*, $[X/H]_{\rm abs}$	25	0.436	2.58×10^{-2}	5			10, 1, 1
log SFR, $[X/H]_{\rm abs}$	18	−0.447	6.52×10^{-2}	4			10, 1, 2
log sSFR, $[X/H]_{\rm abs}$	17	−0.597	1.11×10^{-2}	4			10, 1, 3
log sSFR, log M_*	80	−0.465	1.38×10^{-5}	55	−0.580	3.53×10^{-6}	

Notes. $[X/H]_{\rm abs}$ is the absorption metallicity and $[X/H]_{\rm emi}$ is the emission metallicity. Some rows do not list $r_{\rm s,\,sample}$ and $p_{\rm sample}$ values, because the number of paired parameters is insufficient to perform the correlation tests.

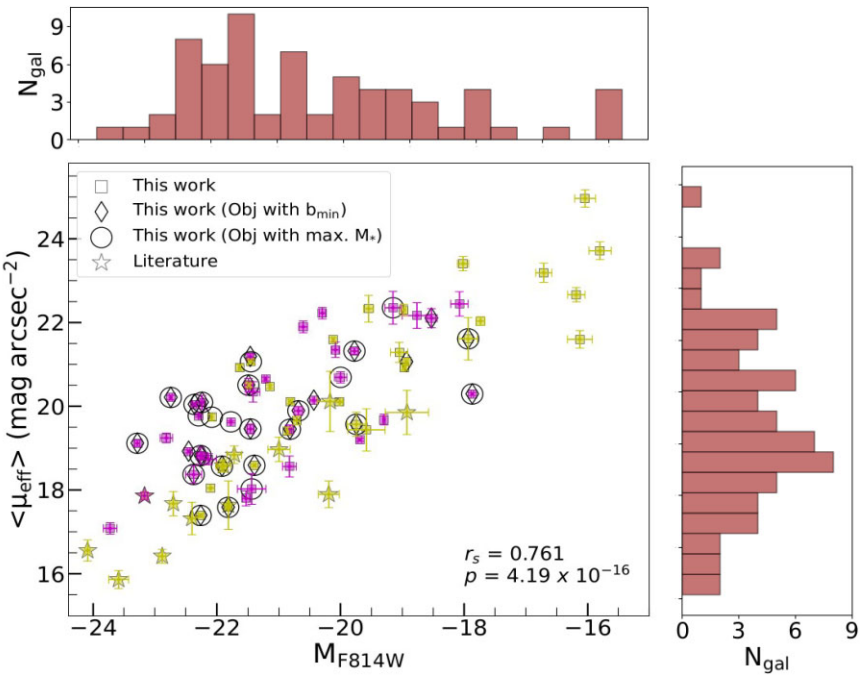

Figure 5. The absolute surface brightness averaged within the effective radius of the galaxies associated with H I absorbers plotted against the absolute magnitude in the UVIS/*F*814*W* band. Sample and literature galaxies are divided into two bins in terms of H I column density using the median value of column density of H I ($N_{\rm HI,\,med} = 6.03 \times 10^{19}$ cm^{-2}). The magenta and yellow symbols denote galaxies with $N_{\rm HI} < N_{\rm HI,med}$ and $N_{\rm HI} \geq N_{\rm HI,med}$, respectively. The diamonds denote galaxies nearest to the quasar sight lines (in impact parameter) from our *HST* measurements, while the open circles denote the most massive galaxies in each quasar field at the redshift of the absorber. The literature galaxies are from Fynbo et al. (2011), Augustin et al. (2018), and Rhodin et al. (2021). For these literature galaxies, we calculated the surface brightness within R_e using the photometric magnitudes listed in the respective papers. The stacked histograms show the distribution of the galaxies in both the axes.

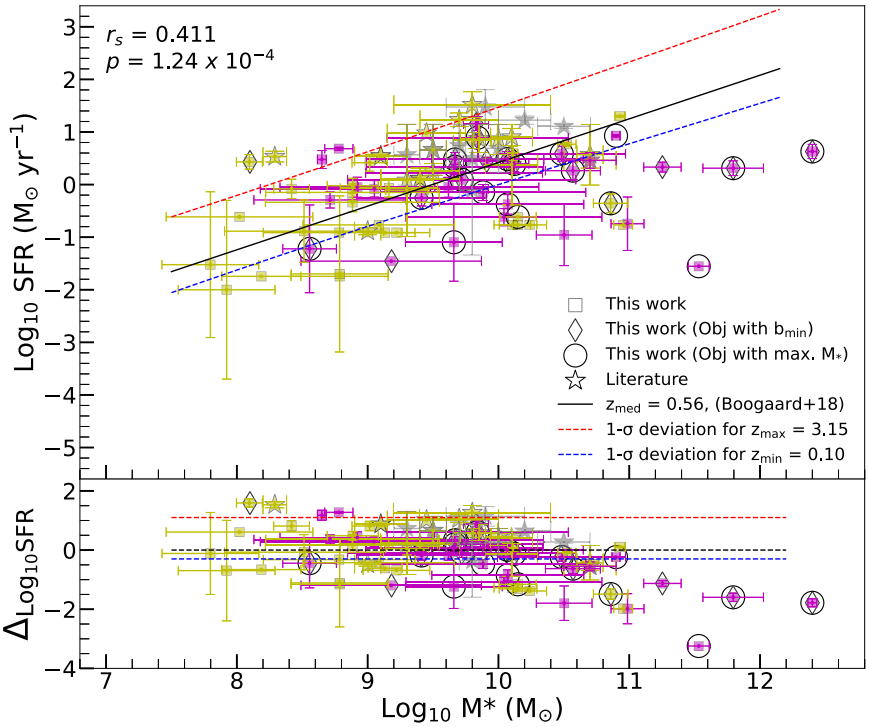

Figure 6. Upper panel: SFR versus stellar mass for galaxies associated with gas-rich absorbers. The grey stars denote galaxies from Zabl et al. (2019) whose H I column density is more uncertain [not based on the actual Ly α absorption profile, but estimated from the Mg II λ2796 equivalent width using the relation from Ménard & Chelouche (2009)]. The yellow and magenta stars denote galaxies from Fynbo et al. (2011), Krogager et al. (2012), Christensen et al. (2014), Augustin et al. (2018), and Rhodin et al. (2021). All other symbols are as in Fig. 5. The solid black line shows the SFMS from Boogaard et al. (2018) at the median redshift of the sample galaxies. The blue and red dashed lines show the 1σ deviations from the SFR–$M*$ relations at z_{min} and z_{max} of the full sample of absorber-associated galaxies (including galaxies from both our MAH sample and the literature). Lower panel: plot of the difference between the observed SFR and the expected SFR from the SFMS at z_{med} taken from Boogaard et al. (2018) at the observed stellar mass versus the stellar mass. The blue and red dashed lines show the difference relative to the SFMS at z_{med} for the lower and upper 1σ SFMS at z_{min} and z_{max}.

the galaxy. A clear positive correlation (r_s = 0.76 and p = 4.19 $\times$ 10^{-16}) is observed, consistent with results from past studies (e.g. McConnachie 2012; Karachentsev, Makarov & Kaisina 2013; Seo & Ann 2022). However, we find no substantial difference between the trends for the lowest and intermediate column density bins. The trend appears to be flatter for the lowest luminosity galaxies, especially for galaxies associated with the highest H I column density absorbers. This finding is consistent with past suggestions that the highest H I column density absorbers may be associated with dwarf galaxies (Kulkarni et al. 2010). We also analysed a plot similar to Fig. 5 by sub-sampling our sample galaxies into two redshift bins using the median redshift of the sample galaxies. No significant differences are observed between z and N_{HI} sub-samples.

4.3.2 *Dependence of SFR on stellar mass*

Fig. 6 shows a plot of the SFR versus stellar mass, revealing a strong correlation with r_s = 0.41 and p = 1.24 $\times$ 10^{-4}. Also shown for comparison is the SFR–M_* relation, i.e. the star formation main sequence (SFMS) for galaxies at z = 0.56, the median redshift of our sample of absorber-associated galaxies (based on the SFMS from Boogaard et al. 2018). Since the SFMS evolves with redshift and our full sample covers a wide redshift range, we show the 1σ deviations from the SFMS relations at z = 0.10 and z = 3.15 (the minimum and maximum redshifts of our full sample).

Most galaxies associated with strong intervening quasar absorbers appear to be consistent with the SFMS within the uncertainties. We note, however, that a small fraction of high-mass galaxies lie below the SFMS. The lower panel of Fig. 6 shows the deviation from the SFMS versus M_*. The deviation seems to be highest for galaxies with the highest stellar mass. Similar conclusions were also reached by Kulkarni et al. (2022). We note, however, that dust corrections for SFRs were not possible for most of these galaxies (12 out of the 14 galaxies with M_* > 10^{10}M$_\odot$ showing >2σ deviation from the SFMS), and the true SFRs for these galaxies could be higher.

4.3.3 *Dependence of stellar mass on Sérsic index and size*

Fig. 7 shows plots of the stellar mass versus the effective radius and Sérsic index. Also shown for comparison is the mass–size scaling relationship for galaxies at 0.50 < z < 0.75 adopted from Ichikawa, Kajisawa & Akhlaghi (2012). M_* appears to be strongly correlated with the effective radius (r_s = 0.49, p = 9.77 $\times$ 10^{-7}). A similar result was found in previous studies (e.g. Ichikawa, Kajisawa & Akhlaghi 2012). A positive correlation is observed between the Sérsic index and stellar mass with r_s = 0.43 and p = 2.51 $\times$ 10^{-4}. The more massive galaxies tend to be more centrally concentrated and therefore earlier-type. Similar results were also observed in previous studies (e.g. van der Wel et al. 2014; Mowla et al. 2019; Lima-Dias et al. 2021). However, we caution that our sample is relatively small, and the correlation between M_* and n is sensitive to the presence of a few galaxies with the largest masses. It seems clear that galaxies with Sérsic index below 1.2 are primarily below 10^{10}M$_\odot$ in stellar mass, while those with higher Sérsic indices span the full mass range,

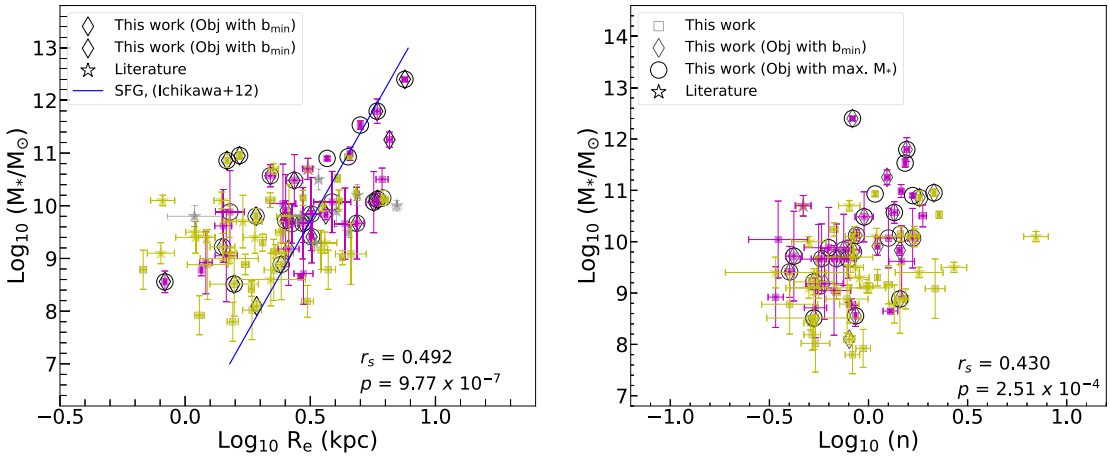

Figure 7. Mass–size and mass–concentration relationships for the galaxies associated with the absorbers. Left panel: plot of stellar mass against the effective radius. The solid blue line is the scaling relationship between the mass and size of SFGs from Ichikawa et al. (2012) with redshifts of $0.50 < z < 0.75$. Right panel: plot of stellar mass against the Sérsic index. The plots suggest that massive galaxies are bigger in size and more concentrated. The grey stars in the left panel are the literature sample from Zabl et al. (2019) whose H I column density is estimated from the Mg II λ2796 equivalent widths using the relation from Ménard & Chelouche (2009). All other symbols are as in Fig. 5.

consistent with observations of a wide mass range among local early-type galaxies (e.g. dwarf spheroidal and giant elliptical galaxies)

To summarize, we have compared the various morphological and stellar properties of our galaxies (which were selected for strong H I absorption) with the properties of the global galaxy population. We find that the absorption-selected galaxies exhibit similar properties as shown by the general population.

4.4 How do stellar and absorption properties relate?

We now examine the stellar properties of the galaxies within the velocity range of ±500 km s^{-1} of the absorption redshift with the absorption properties. We only include the absorbers with reliable metallicities for comparisons of absorption metallicities and stellar properties of the galaxies. To perform these comparisons, we selected galaxies with the smallest impact parameters from the quasar sightlines and the most massive galaxies in each quasar field detected within ±500 km s^{-1} of the absorption redshift. We note that it is not possible to consider all the galaxies in such cases or even use the average values of the stellar properties of all the galaxies since doing so would either underestimate or overestimate the true values, given that the impact parameters of the individual galaxies are different.

4.4.1 Impact parameter and galactic effective radius

Fig. 8 shows the impact parameter versus the effective radius for our galaxies and other absorption-selected galaxies from the literature. For reference, the red and blue dashed lines correspond to $b = R_{vir}$, and $b = R_{vir}/2$, respectively, assuming the approximate relation between the effective radius and the Virial radius (Kravtsov 2013). Most of the sample galaxies (∼85 per cent) lie below $b = R_{vir}$, and more than half of the sample galaxies (∼59 per cent) lie below $b = R_{vir}/2$. All of the galaxies at the smallest impact parameters (i.e. the most probable host galaxies) are located below $b = R_{vir}$, while almost all massive galaxies (∼96 per cent) are present below the red dashed line, as shown in the Fig. 8. Given the approximate relation between the effective radius and the Virial radius (Kravtsov 2013), b/R_e ∼70 corresponds to $b \sim R_{vir}$. It is thus interesting to note that most of the galaxies have impact parameters below R_{vir} and that the galaxies with impact parameters larger than $\sim 0.3\ R_{Vir}$ are almost all below the sub-DLA limit in H I column density (Noterdaeme et al. 2014). While most DLAs and sub-DLAs are associated with galaxies at impact parameters less than $0.2\ R_{vir}$, a small fraction (∼26 per cent) of sample galaxies have impact parameters in the range of $0.5\ R_{vir}$ to R_{vir}. All of the galaxies from the literature lie below $b = R_{vir}/2$. This suggests that while these gas-rich absorbers usually trace regions close to galaxy centres, they occasionally trace the CGM at large distances extending out to the Virial radius.

4.4.2 Dependence of Mg II λ 2796 rest-frame equivalent width on stellar mass

Studies of the interdependence of the Mg II λ 2796 absorption strength and the galaxy's stellar properties have reached different conclusions. Bordoloi et al. (2011) reported that the Mg II equivalent widths [estimated from low-resolution spectra of zCOSMOS galaxies, obtained with the Visible Multi-Object Spectrograph (VIMOS) on the VLT, by fitting a single Gaussian profile across the Mg II λ 2796 and λ 2803 lines] increase with stellar mass for blue galaxies at lower impact parameter ($b < 50$ kpc). However, such dependence is absent in the red galaxies and even in blue galaxies with larger impact parameters ($b > 65$ kpc). Nielsen, Churchill & Kacprzak (2013) suggested that more massive galaxies have larger Mg II equivalent width in the MAGIICAT sample, based on a positive correlation between the *K*-band luminosity (assumed to be a proxy of M_*) and the Mg II equivalent width.

For impact parameters smaller than 50 kpc, Lan, Ménard & Zhu (2014) showed that the Mg II λ 2796 equivalent width shows a positive correlation with $M*$ for SFGs but not for passive galaxies. Taking the larger dispersion values in median Mg II λ 2796 equivalent widths, Rubin et al. (2018) found that the median Mg II equivalent widths increase with the stellar mass for blue galaxies at a transverse distance $30\ \text{kpc} < R_\perp < 50\ \text{kpc}$; however, the median Mg II λ 2796 equivalent widths values for red galaxies are found to be smaller compared to those for high-mass blue galaxies. Including both detections and upper limits in Mg II λ 2796 equivalent widths measurements, Dutta et al. (2020) reported a weak positive correlation between Mg II λ 2796 equivalent widths and $M*$ in the MAGG sample.

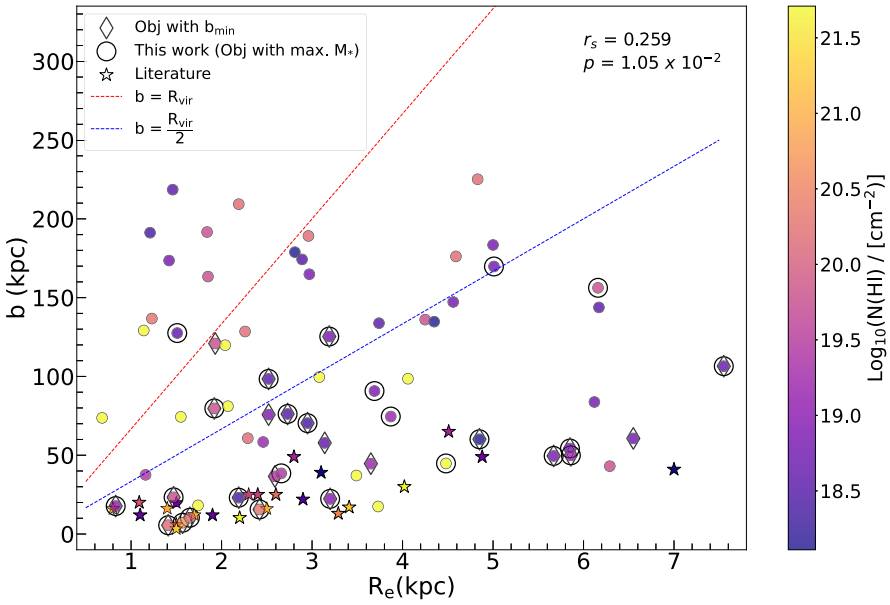

Figure 8. The effective radii of the absorber-associated galaxies plotted against the impact parameter colour-coded by column density of neutral hydrogen of the absorber. The diamonds denote the sample galaxies that lie closest to the quasar sightlines, while the open circles denote the most massive galaxies in the field of each quasar at the redshift of the absorber. The stars denote the literature sample galaxies. The red and blue dashed lines correspond to b = R_{vir}, and b = $R_{vir}/2$, respectively, taking the approximate relation between the effective radius and the virial radius. Most of the sample galaxies are found at or within R_{vir} and more than half of the sample galaxies are found at or within the half of R_{vir}. All the galaxies that are closest to the quasar sightlines are within the virial radius. The higher H I column density absorbers appear to be tracing regions relatively close to the galactic centres and fewer gas-rich absorbers appear to be tracing the CGM at large distances.

For our MAH sample and literature galaxies, we find a weak negative correlation (r_s = -0.27, p = 4.86 $\times 10^{-2}$) between the Mg II λ 2796 equivalent widths and stellar mass. Part of the reason for the difference between this trend and the weak or positive relations found for Mg II absorbers seems to be the difference in the selection techniques. Our sample absorbers are selected by high N_{HI}, and therefore have higher Mg II λ 2796 equivalent widths. For example, ∼ 70 per cent of the absorbers in our sample have Mg II λ 2796 rest equivalent widths >0.5 Å, while only < 15 per cent of the absorbers in the sample of Dutta et al. (2021) fall in this category. Moreover, ∼ 60 per cent of the galaxies in our sample are at impact parameters less than 100 kpc, while only < 10 per cent of the galaxies in the sample of Dutta et al. (2021) fall in this category. We also note that our M_* values have substantial uncertainties, making a robust detection of the trend difficult. Fig. 9 shows plots of Mg II λ 2796 absorption strengths versus the stellar mass. The H I column density is known to be positively correlated with the Mg II and Fe II absorption strengths (e.g. Rao et al. 2006). Furthermore, the H I column density is negatively correlated with the stellar mass and with metallicity, suggesting that the lower N_{HI} absorbers are associated with more massive galaxies that have had high past star formation and gas consumption (Kulkarni et al. 2010; Augustin et al. 2018). The negative correlation seen in the Fig. 9 is thus expected.

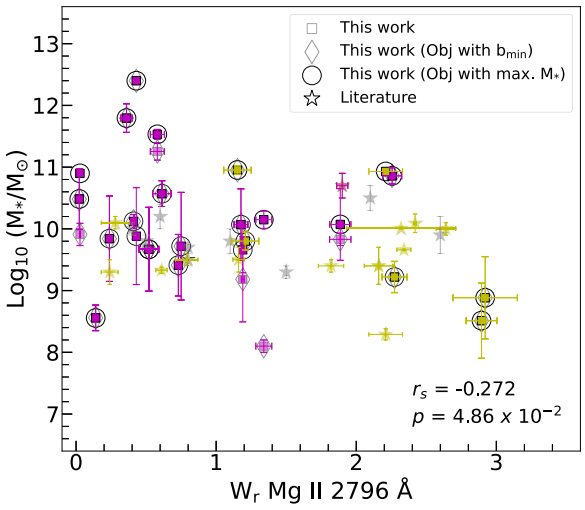

Figure 9. The rest-frame equivalent width of Mg II λ 2796 plotted against the stellar mass. All symbols are as in Fig. 5. A tentative negative correlation is seen: more massive galaxies are associated with lower metal line strengths. Such a trend would be consistent with the fact that the stellar mass of the galaxy is anticorrelated with the column density of H I gas (e.g., Augustin et al. 2018), while N_{HI} is positively correlated with the equivalent width of the Mg II line (e.g., Rao et al. 2006).

4.4.3 Dependence of metallicity on stellar properties

The left panels of Fig. 10 show plots of absorption metallicities versus stellar properties (M_*, SFR and sSFR) of the galaxies. For most cases, we use absorption metallicities based on Zn, which is less depleted on dust grains. For one absorber, we use the dust-free absorption metallicity inferred from multiple elements using the method of Jenkins (2009) based on depletion trends observed in the local ISM of the Milky Way. The right panels of Fig. 10 show similar plots, but for the emission metallicities [from Weng et al. (2023) for our sample and from Christensen et al. (2014), Augustin et al. (2018), and Rhodin et al. (2018) for the literature sample]. Also shown, for reference, in the left and right upper panels of Fig. 10 are the mass–metallicity relation (MZR) for SFGs at 0.5 < z < 1.0 and the 1σ uncertainties in this relation (Ly et al. 2016).

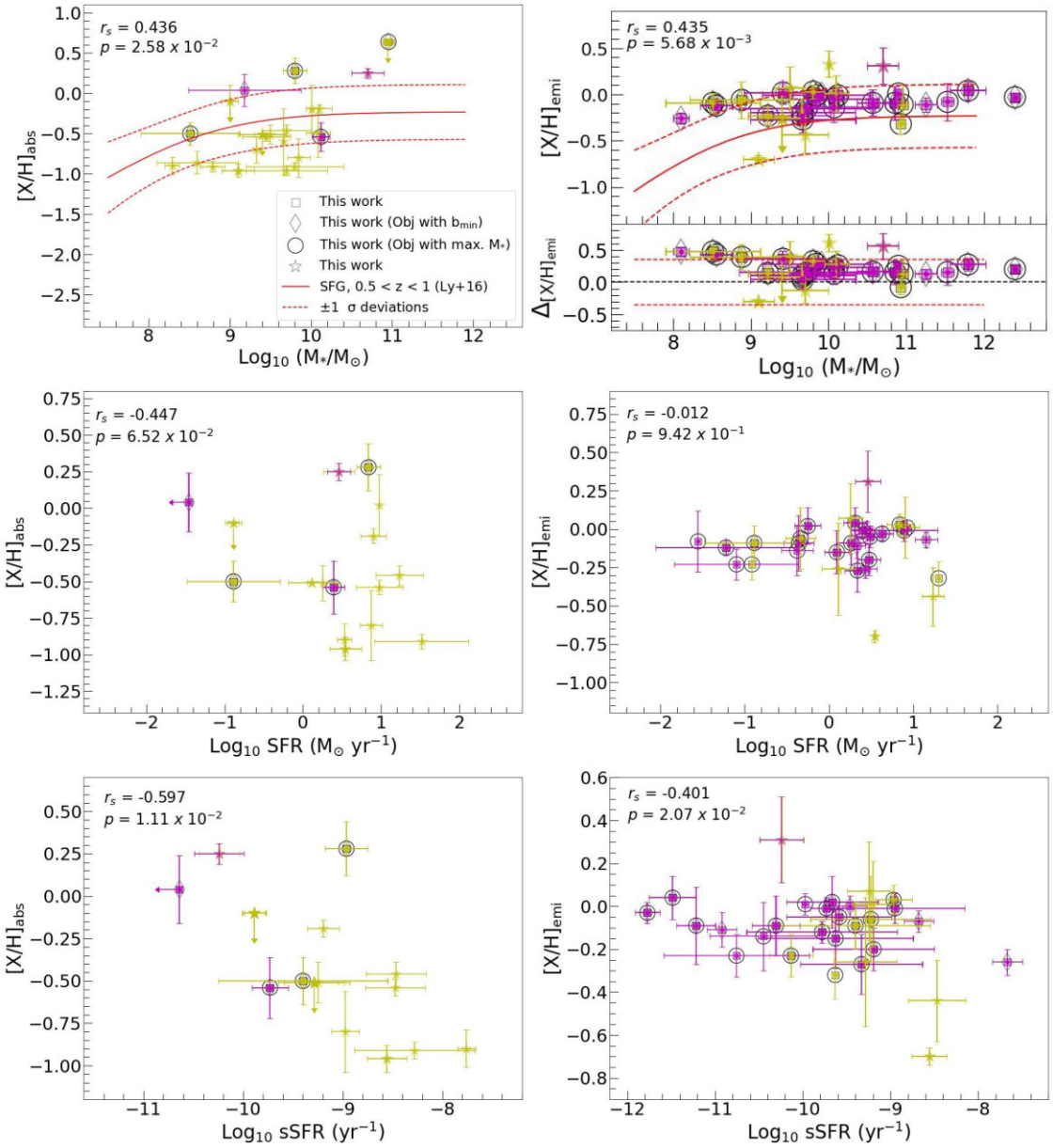

Figure 10. Absorption and emission metallicities plotted against stellar properties of gas-rich galaxies. Left panel: absorption metallicities plotted against the stellar mass, SFR, and specific SFR (from top to bottom). All symbols are as in Fig. 5. The absorption metallicities are based on Zn for most cases, while for one absorber, we adopt dust-free absorption metallicity. Right panel: emission metallicities plotted against the stellar mass, SFR, and specific SFR (from top to bottom). The solid and dashed black lines show, respectively, the MZR for $0.5 < z < 1.0$ from Ly et al. (2016) and the $\pm 1\sigma$ uncertainties in this relation. The subpanel at the bottom of the upper right panel shows the difference between the observed emission metallicities and the expected emission metallicities from the MZR (Ly et al. 2016) plotted versus the stellar mass.

The bottom sub-panel in the upper right panel shows the difference in the observed emission metallicities and the expected emission metallicities based on the MZR from Ly et al. (2016) at the observed stellar mass. It is clear that both the absorption-based metallicity (away from the galaxy centre, at the impact parameter of the corresponding quasar sight line) and the emission-based metallicity (typically at the galaxy centre) are positively correlated with the stellar mass, and are generally consistent with the MZR for SFGs.

The middle panels of Fig. 10 show plots of the absorption and emission metallicity versus the SFR. No correlation is observed between metallicity (both absorption and emission metallicity) and SFR. The bottom panels of Fig. 10 show plots of the absorption and emission metallicity versus the specific star formation rate (sSFR). Both absorption and emission metallicity are negatively correlated with the sSFR. This suggests that the low-metallicity absorbers are associated with galaxies that are forming stars (and consuming gas) more vigorously. However, they are less enriched due to low past star formation activity. While the plot suggests that the negative correlation is mostly driven by the presence of literature galaxies, it is essential to expand the sample to verify this correlation.

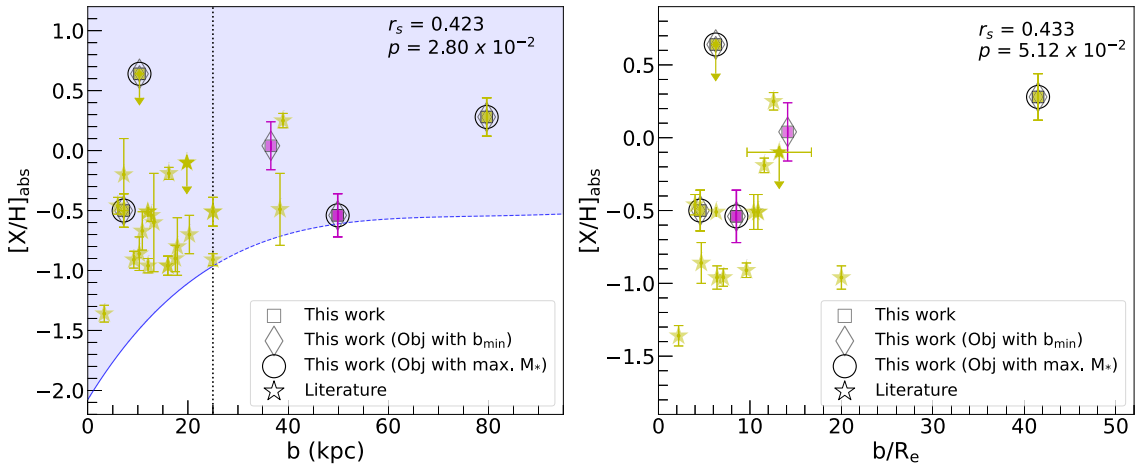

Figure 11. Absorption metallicities plotted versus the impact parameter (left) and the normalized impact parameter (right). All symbols are as in Fig. 5. The light blue region below the solid blue line in the left panel figure denotes the simulated distribution of impact parameters plotted against the absorption metallicities using the model described in Fynbo et al. (2008) for the DLA galaxies at $z = 3$ and is taken from Krogager et al. (2012). Extrapolating the model's prediction, the region is further extended up to the impact parameters of 100 kpc to include the sample galaxies detected at the larger impact parameters and is denoted by a light blue region below the dashed blue line. The trends suggest that metal-poor strong H I absorbers are found in smaller haloes and therefore at smaller impact parameters (Krogager et al. 2012).

4.4.4 Dependence of metallicity on impact parameter and galaxy's size

Fig. 11 shows plots of the metallicities of the absorption-selected galaxies versus the impact parameter and the normalized impact parameter for galaxies from our sample and the literature. To place these in context, we use a model for the metallicity–size relation for DLAs suggested by Fynbo et al. (2008). In this simple model, galaxies are assigned a size, metallicity, and metallicity gradient based on their luminosities. The metallicity distributions of the quasar DLAs and GRB DLAs are predicted using the luminosity function of UV-selected galaxies (Lyman Break Galaxies), a metallicity versus luminosity relation, and the radial distribution of H I gas along with luminosity. Using such a model prediction, Krogager et al. (2012) generated 4000 simulated data points to compare to the measured data points. The light blue region under the solid blue line in the right panel of Fig. 11 shows these 4000 simulated data points. For further details, see e.g. Krogager et al. (2012). We extended the region to impact parameters of 100 kpc to include our sample galaxies. To do so, we extrapolated the metallicity versus impact parameter relationship predicted by those simulation points. The light blue region under the dashed blue line in the Fig. 11 shows the extrapolated region.

Both panels of Fig. 11 suggest that the metallicity is higher for galaxies sampled at higher impact parameters. This result is in agreement with previous studies (e.g. Krogager et al. 2012, 2017), and would be consistent with the model expectation (Fynbo et al. 2008). This suggests that the metal-poor systems are found in smaller haloes and therefore detectable only in galaxies at lower impact parameters (Krogager et al. 2012).

4.4.5 Dependence of H I column density on impact parameter and galaxy size

Fig. 12 shows the impact parameter normalized by the effective radius and the effective radius plotted versus the H I column density. A negative correlation ($r_s = -0.56$ and $p = 2.00 \times 10^{-4}$) is observed between the normalized impact parameter and the H I column density. The effective radius of the absorbing galaxies also shows a strong negative correlation ($r_s = -0.52$ and $p = 6.00 \times 10^{-4}$) with H I column density. This shows that galaxies associated with higher H I absorbers are smaller in size, and therefore likely to show strong absorption at small impact parameters. Indeed, all galaxies in the current sample associated with DLAs have effective radii smaller than 3 kpc, while all galaxies with $R_e > 3$ kpc are associated with lower H I column density absorbers. This finding is consistent with past suggestions that DLAs are associated with dwarf galaxies (e.g. York et al. 1986; Kulkarni et al. 2010).

4.4.6 Relation between H I column density and surface density of star formation

Fig. 13 shows plots of the surface densities of the SFR and sSFR averaged within the effective radius versus the column density of H I. In the upper two panels, the galaxies are binned into two groups by stellar mass (above and below the median stellar mass $\log M*_{med} = 9.67$). In the lower two panels, the galaxies are binned into two groups by redshift ($z < 1$ and $z \geq 1$). For comparison with local galaxies, we also show the relationship observed between the surface densities of SFR and H I (Kennicutt 1998) for low-redshift spirals (what we refer to as the 'atomic Kennicutt–Schmidt (KS) relation'). This relation is based on the best fit ($\log \Sigma_{SFR} = 1.02 \log \Sigma_{HI} - 2.89$) between the tabulated values of Σ_{SFR} and Σ_{HI} listed in Kennicutt (1998). We use this relation (which translates to $\log \Sigma_{SFR} = 1.02 \log N_{HI} - 23.36$) rather than the standard KS relation between Σ_{SFR} and Σ_{gas} since the latter also includes molecular gas, and molecular gas measurements are not available for most of the absorber-selected galaxies plotted in Fig. 13 (besides the few objects observed so far in CO emission with ALMA).

The upper right panel of Fig. 13 shows that Σ_{sSFR} is positively correlated with the H I column density. The Spearman rank order correlation test gives $r_s = 0.42$ and $p = 8.30 \times 10^{-3}$ between N_{HI} and Σ_{sSFR} (although we note that this relation is not significant if only our sample galaxies are considered.) The correlation between Σ_{SFR} and N_{HI} (shown in the upper left panel of Fig. 13) is not as significant even after including the literature galaxies, with $r_s = 0.29$ and $p = 6.65 \times 10^{-2}$. This finding seems to be at odds

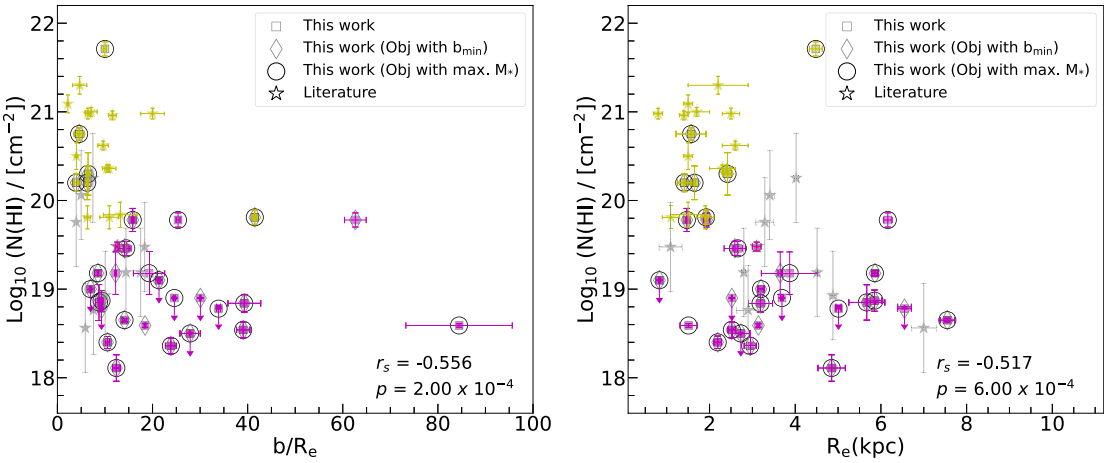

Figure 12. The normalized impact parameter (b/R_e) and the effective radius plotted against the column density of H I gas. Left panel: The plot of b/ R_e against N_{HI} shows that the H I column density is higher for galaxies found at lower impact parameters to the quasar's sightline. At the same time, there is low H I column density in the regions located at larger distances. Right panel: plot of R_e against N_{HI}. The gas-rich galaxies are smaller in size than the gas-poor galaxies. All symbols are as in Fig. 5. The stars denote the literature values taken from Fynbo et al. (2011), Krogager et al. (2012), Christensen et al. (2014), Augustin et al. (2018), and Rhodin et al. (2021). The grey stars denote the literature galaxies from Zabl et al. (2019) whose H I column density is estimated from the Mg II λ2796 equivalent widths using the relation from Ménard & Chelouche (2009).

with the previous suggestions based on simulations (e.g. Nagamine, Springel & Hernquist 2004) that DLAs follow the KS law.

Indeed, most of the galaxies associated with the absorbers from our sample and the literature lie substantially above the 'atomic KS relation'. If taken at face value, this suggests that the absorption-selected galaxies (which have $z_{med} \sim 0.8$) have more efficient star formation compared to the nearby galaxies. However, this apparent discrepancy may also be caused in part by the fact that the local 'atomic KS relation' is based on observations of 21-cm emission (which is usually far less sensitive to low H I column densities than the Ly α absorption line technique used for the quasar absorber sample).

We also note that the galaxies with stellar mass greater than the median mass are located farther away from the 'atomic KS' relation in the upper left panel of Fig. 13, as compared to lower mass galaxies. This suggests that the more-massive absorption-selected galaxies have more efficient star formation, allowing them to reach comparable SFRs in lower H I column density regions.

The high values of Σ_{SFR} compared to the KS relation for the galaxies in our sample and the literature seen in Fig. 13 may appear surprising, given the findings of earlier studies based on indirect estimates of SFR surface density that the star formation efficiency in DLAs at $z \geq 1$ is 1–3 per cent of that predicted by the KS relation (e.g. Wolfe & Chen 2006; Rafelski, Wolfe & Chen 2011; Rafelski et al. 2016). The latter measurements are also shown in the left panels of Fig. 13 for comparison. A substantial fraction of our galaxies have $18 < \log N_{HI} < 20$. But even focusing on just the absorbers with $\log N_{HI} \geq 20.3$ (i.e. the DLAs) in our sample, the star formation efficiency of the absorber-associated galaxies (with a median redshift of ∼1.01) still appears to be comparable to or (for some galaxies) substantially higher than predicted by the KS relation.

The large difference between our values of Σ_{SFR} and those in the past DLA studies may result from the fact that, unlike our the study, the past studies were based not on direct SFR measurements for galaxies associated with DLAs, but on measurements in the outskirts of isolated SFGs and on the assumption that the latter are related to DLAs. It is also noteworthy in this context that the surface brightness of the galaxies associated with DLAs detected in our sample and those from the literature are in fact several magnitudes brighter than the upper limit of 29 mag arcsec^{-2} estimated in prior studies of star formation efficiency in DLAs at $z \sim 3$ (Wolfe & Chen 2006; Rafelski et al. 2011). We note, however, that we cannot make a precise statement about the agreement between those DLAs and the simulation data due to the limited number of simulated galaxies with $N_{HI} > 10^{21}$ cm^{-2}. The ability of IFS studies to reveal SFGs associated with DLAs (and lower H I column density absorbers) demonstrated by our MAH sample and other IFS studies in the literature indeed mark a huge improvement in detecting star formation in galaxies associated with gas-rich quasar absorbers compared to past searches. We also note, in passing, that the previous studies of the SFR surface density in DLAs mentioned above (e.g. Nagamine et al. 2004; Rafelski et al. 2016) adopted the original KS relation for Σ_{SFR} versus Σ_{gas} instead of the 'atomic' version of this relation Σ_{SFR} versus Σ_{HI}.

To examine whether the star formation efficiency of absorber-selected gas-rich galaxies may have increased dramatically at $z < 1$, we compare the Σ_{SFR} versus log N_{HI} trends for galaxies with $z < 1$ and galaxies at $z \geq 1$ in the lower panels of Fig. 13. The lower redshift galaxies appear to have comparable SFR surface densities for lower H I column densities. This suggests a higher star formation efficiency of absorber-selected galaxies at $z < 1$ compared to those at $z \geq 1$. Also shown for comparison in Fig. 13 are simulated galaxies at $z = 0.5$, based on an analysis of the data obtained from the Illustris TNG simulations (Marinacci et al. 2018; Naiman et al. 2018; Nelson et al. 2018; Pillepich et al. 2018; Springel et al. 2018). These state-of-the-art cosmological simulations incorporate essential physical processes pertinent to the formation and evolution of galaxies, such as gravity, hydrodynamics, gas cooling, star formation, stellar feedback, black hole feedback, and more. In this study, we employ the highest resolution version of the TNG100 simulation, executed within a ∼ 100 Mpc box. Haloes are initially identified by employing the Friends-of-Friends (FOF) algorithm (Davis et al. 1985). Galaxies, regarded as substructures, are recognized as gravitationally bound assemblies of particles within these FOF haloes performing the SUBFIND algorithm (Springel et al. 2001). Each FOF halo encompasses a central galaxy, generally the most massive galaxy within that halo, and all additional galaxies within the halo are labelled as satellites.

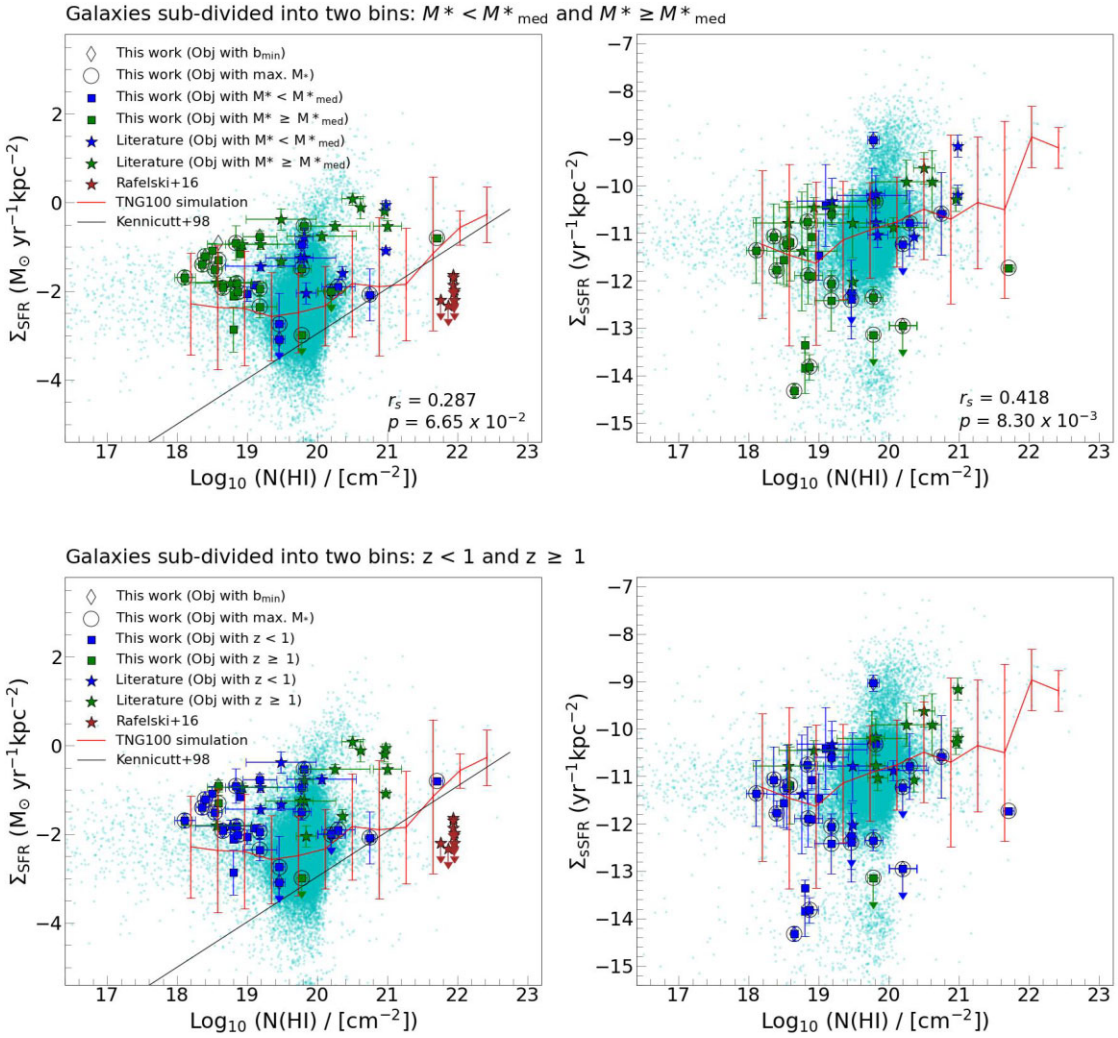

Figure 13. The surface densities of SFR (left panels) and sSFR (right panels) measured within the effective radius plotted versus the H I column density. In the top panels, the galaxies are subdivided into two bins using the median value of the stellar mass. Galaxies with log $M*$ < log $M*_{\rm med}$ are denoted as blue squares and galaxies with log $M*$ ≥ log $M*_{\rm med}$ are denoted as green squares. The bottom panels show similar plots where the galaxies are subdivided into two bins in terms of galaxies' redshift. The blue symbols show galaxies with $z_{\rm gal}$ < 1, while the green symbols show galaxies with $z_{\rm gal}$ ≥ 1. The diamonds denote galaxies nearest to the quasar sight lines from our *HST* measurements, while the open circles denote the most massive galaxies in the field of each quasar at the redshift of the absorber. One of the sample galaxies does not have $M*$ measurement and is denoted by an unfilled diamond. The stars are the literature values taken from Fynbo et al. (2011), Krogager et al. (2012), Christensen et al. (2014), Rafelski et al. (2016), Augustin et al. (2018), Ma et al. (2018), and Rhodin et al. (2021). In the left panels, the solid black line is the KS relationship for nearby galaxies taken from Kennicutt (1998), while in all panels, the solid red line is the median value of the surface densities obtained from the TNG100 simulation. The solid red vertical lines denote 1σ uncertainties in the median value. The cyan dots are the simulated galaxies at $z = 0.5$. No correlation is observed between SFR surface density and H I column density but a positive correlation exists between sSFR surface density and H I column density. Absorption-selected galaxies have a higher star formation efficiency than predicted by the KS law for local galaxies. See the text for more details.

Properties of galaxies, including stellar masses and SFRs, are taken from the principal TNG galaxy catalogues. These are measured within the stellar half-mass radius by utilizing the particle data of the simulation. Furthermore, the neutral hydrogen (H I) content of TNG galaxies has been extracted from catalogues provided by Diemer et al. (2018), based on the analytic model of Sternberg et al. (2014), where they use an optimized post-processing framework for estimating the abundance of atomic and molecular hydrogen. This method uses the surface density of neutral hydrogen and the ultraviolet (UV) flux within the Lyman-Werner band, with all computations being performed through face-on projections within a two-dimensional model. The UV radiation emitted from young stars is modelled assuming a constant escape fraction and optically thin propagation across the galaxy. The simulation demonstrates a relatively satisfactory agreement with the measurements of the SFR surface density based on emission-line observations for galaxies from both our sample and the literature shown in Fig. 13 (and, like these data, also lie substantially above the upper limits for the DLAs from past studies).

The agreement between the simulated and observed data appears to be better for the sSFR surface density than for the SFR surface density, as seen in the right panels of Fig. 13. This difference may result from the differences in the stellar mass distributions for the simulated and observed galaxies. The stellar mass distribution

of the observed galaxies (from our sample and the literature) peaks around log $M_* = 9.67$ and shows fewer low-M_* galaxies compared to the distribution for the simulated galaxies. The higher M_* galaxies have lower $\Sigma_{\rm sSFR}$ (as expected from the negative correlation between sSFR and M_*, see Table 5), giving better consistency between the $\Sigma_{\rm sSFR}$ versus $M*$ trends for the simulated and observed galaxies, compared to the median $\Sigma_{\rm SFR}$ versus $M*$ trends.

To summarize, we find interdependence between the stellar properties and the absorption properties. In particular, the H I column density and the absorption metallicity show correlations with $M*$, ssfr, $\Sigma_{\rm sSFR}$, but not with the SFR and $\Sigma_{\rm SFR}$.

5 SUMMARY AND CONCLUSIONS

We have analysed the morphological and stellar properties of 66 galaxies detected within $\pm$500 km s^{-1} of the redshifts of strong intervening quasar absorbers at $0.2 \lesssim z \lesssim 1.4$ with $N_{\rm HI} > 10^{18}$ cm^{-2} (that also have MUSE and/or ALMA data). The structural parameters of these absorption-selected galaxies were determined using GALFIT. The galaxies were found to have Sérsic indices ranging from 0.3 to 2.3 and effective radii ranging from 0.7 to 7.6 kpc. The k-corrected absolute magnitudes of these galaxies range from -15.8 to -23.7 mag. Our main findings are as follows:

(i) The absolute (rest-frame) surface brightness shows a strong positive correlation with the galaxy luminosity. The trend appears flatter at lower luminosities for galaxies associated with high H I column density absorbers. This suggests dwarf galaxies are associated with high H I column densities.

(ii) The SFR correlates well with the stellar mass. Most galaxies associated with intervening quasar absorbers are consistent with the SFMS.

(iii) Larger galaxies are found to be more massive compared to smaller galaxies. Furthermore, massive galaxies are more centrally concentrated, as observed for nearby galaxies. Overall the absorption-selected galaxies follow similar trends as those shown by the general galaxy population.

(iv) For most ($\sim$85 per cent) of the galaxies in our sample, the impact parameters are smaller than the virial radius. Most of the sight lines with high $N_{\rm HI}$ in our sample probe the CGM of the associated galaxies at impact parameters less than half the virial radius, and only a small fraction have impact parameters larger than the virial radius.

(v) The rest-frame equivalent widths of Mg II λ 2796 show a negative correlation with stellar mass. Such a trend suggests that lower $N_{\rm HI}$ absorbers are associated with more massive galaxies that have undergone high past star formation and gas consumption activity.

(vi) The absorption metallicity and emission metallicity show a positive correlation with the stellar mass for many of the absorption-selected galaxies and are consistent with the MZR for SFGs. While the metallicity shows no correlation with SFR, the metallicity is negatively correlated with the specific SFR, suggesting that the low-metallicity absorbers are associated with galaxies with vigorous current star formation but low past star formation activity.

(vii) Metallicity appears to be positively correlated with the impact parameter and normalized impact parameter. This suggests that metal-poor galaxies are found in smaller haloes and are therefore detectable in galaxies at smaller impact parameters.

(viii) The H I column density is negatively correlated with the normalized impact parameter and the effective radius of the galaxies. This shows that galaxies associated with higher $N_{\rm HI}$ absorbers are smaller in size and therefore likely to show strong absorption at small impact parameters.

(ix) The sSFR surface density is positively correlated with the H I column density, but no correlation is seen between SFR surface density and H I column density. Furthermore, the $\Sigma_{\rm SFR}$ for the absorber-associated galaxies is substantially higher than predicted from the atomic KS relation for nearby galaxies, suggesting higher star formation efficiency in the absorber-selected galaxies. The SFR surface density is also substantially higher than the upper limits on $\Sigma_{\rm SFR}$ for DLAs estimated in past studies. Moreover, the star formation efficiency for absorber-associated galaxies at $z < 1$ appears to be higher than for those at $z \geq 1$.

The overall conclusions from our results are as follows: the stellar and morphological properties of absorption-selected galaxies are consistent with the SFMS of galaxies and show the MZR. Furthermore, the higher H I column density absorbers are associated with smaller galaxies in smaller haloes that have generally not experienced much star formation in the past and have thus remained metal-poor. However, these galaxies associated with the higher $N_{\rm HI}$ absorbers have more active current star formation and exhibit higher surface densities of star formation and gas consumption. Our study also reveals that a substantial fraction of gas-rich quasar absorbers arises in groups of galaxies.

Our study of structural and stellar properties of 66 associated galaxies associated with gas-rich quasar absorbers has thus allowed us to search for correlations between a variety of morphological, stellar, and gas properties. However, our sample is still relatively small. Increasing the number of absorption-selected galaxies with measurements of the various properties with future MUSE, ALMA, and *HST* observations is essential to more robustly establish the trends suggested by our study and to fully interpret their implications for the evolution of galaxies and their CGM.

ACKNOWLEDGEMENTS

We thank the anonymous referee for constructive comments that helped to improve this manuscript. AK and VPK acknowledge support from a grant from the Space Telescope Science Institute for GO program 15939 (PI: Péroux). AK and VPK also acknowledge additional partial support from US National Science Foundation grant AST/2007538 and NASA grants NNX17AJ26G and 80NSSC20K0887 (PI: Kulkarni). GK and SW acknowledge the financial support of the Australian Research Council through grant CE170100013 (ASTRO3D). MA acknowledges funding from the Deutsche Forschungsgemeinschaft (DFG) through an Emmy Noether Research Group (grant number NE 2441/1-1). We also thank the International Space Science Institute (ISSI) (https://www.issibern.ch/) for financial support. This research used the following python packages: ASTROPY, a community-developed core Python package for Astronomy (e.g. Astropy Collaboration 2013; Collaboration 2018), MATPLOTLIB (Hunter 2007), PANDAS (McKinney et al. 2010), PHOTUTILS (Bradley et al. 2022), and NUMPY (Harris et al. 2020).

DATA AVAILABILITY

Data directly related to this publication and its figures can be requested from the authors. The raw data can be downloaded from the public archives. The TNG simulation (Nelson et al. 2019) is publicly available at https://www.tng-project.org/.

REFERENCES

Arnouts S., Cristiani S., Moscardini L., Matarrese S., Lucchin F., Fontana A., Giallongo E., 1999, MNRAS, 310, 540
Astropy Collaboration, 2013, A&A, 558, A33
Augustin R. et al., 2018, MNRAS, 478, 3120
Bacon R. et al., 2010, in McLean I. S., Ramsay S. K., Takami H.eds, Proc. SPIE Conf. Ser. Vol. 7035, Ground-based and Airborne Instrumentation for Astronomy III. SPIE, Bellingham, p. 773508
Bashir W., Zafar T., Khan F. M., Chishtie F., 2019, New Astron., 66, 9
Berg T. A. M. et al., 2016, MNRAS, 463, 3021
Berg T. A. M. et al., 2017, MNRAS, 464, L56
Berg M. A. et al., 2023, ApJ, 944, 101
Bergeron J., 1986, A&A, 155, L8
Bergeron J., Boissé P., 1991, A&A, 243, 344
Bertin E., Arnouts S., 1996, A&AS, 117, 393
Blanton M. R., Roweis S., 2007, AJ, 133, 734
Boisse P., Le Brun V., Bergeron J., Deharveng J.-M., 1998, A&A, 333, 841
Boogaard L. A. et al., 2018, A&A, 619, A27
Bordoloi R. et al., 2011, ApJ, 743, 10
Bouché N. et al., 2012, MNRAS, 419, 2
Bouché N., Murphy M. T., Kacprzak G. G., Péroux C., Contini T., Martin C. L., Dessauges-Zavadsky M., 2013, Science, 341, 50
Bradley L. et al., 2022, astropy/photutils: 1.5.0, Zenodo, available at: https://doi.org/10.5281/zenodo.6825092
Buta R. J., 2013, in Oswalt T. D., Keel W. C., eds, Planets, Stars, and Stellar Systems, Vol. 6. Springer, Dordrecht
Carollo C. M. et al., 2013, ApJ, 773, 112
Chen H.-W. et al., 2020, MNRAS, 497, 498
Christensen L., Møller P., Fynbo J. P. U., Zafar T., 2014, MNRAS, 445, 225
Chun M. R., Kulkarni V. P., Gharanfoli S., Takamiya M., 2010, AJ, 139, 296
Churchill C. W., 2001, ApJ, 560, 92
Collaboration T. A., 2018, astropy v3.1: a core python package for astronomy, Zenodo, available at: https://zenodo.org/record/2556700
Curti M., Cresci G., Mannucci F., Marconi A., Maiolino R., Esposito S., 2017, MNRAS, 465, 1384
Davis M., Efstathiou G., Frenk C. S., White S. D. M., 1985, ApJ, 292, 371
Diemer B. et al., 2018, ApJS, 238, 33
Dutta R. et al., 2020, MNRAS, 499, 5022
Dutta R. et al., 2021, MNRAS, 508, 4573
Fossati M. et al., 2019, MNRAS, 490, 1451
Fumagalli M., O'Meara J. M., Prochaska J. X., 2016, MNRAS, 455, 4100
Fynbo J. P. U., Prochaska J. X., Sommer-Larsen J., Dessauges-Zavadsky M., Møller P., 2008, ApJ, 683, 321
Fynbo J. P. U. et al., 2011, MNRAS, 413, 2481
Graham A. W., Driver S. P., 2005, Publ. Astron. Soc. Aust., 22, 118
Hamanowicz A. et al., 2020, MNRAS, 492, 2347
Harris C. R. et al., 2020, Nature, 585, 357
Hartoog O. E., Fynbo J. P. U., Kaper L., De Cia A., Bagdonaite J., 2015, MNRAS, 447, 2738
Häußler B., Barden M., Bamford S. P., Rojas A., 2011, in Evans I. N., Accomazzi A., Mink D. J., Rots A. H.eds, ASP Conf. Ser. Vol. 442, Astronomical Data Analysis Software and Systems XX. Astron. Soc. Pac. San Francisco, p. 155
Hilz M., Naab T., Ostriker J. P., 2013, MNRAS, 429, 2924
Hunter J. D., 2007, Comput. Sci. Eng., 9, 90
Ichikawa T., Kajisawa M., Akhlaghi M., 2012, MNRAS, 422, 1014
Ilbert O. et al., 2006, A&A, 457, 841
Jenkins E. B., 2009, ApJ, 700, 1299
Kacprzak G. G., Churchill C. W., Evans J. L., Murphy M. T., Steidel C. C., 2011, MNRAS, 416, 3118
Karachentsev I. D., Makarov D. I., Kaisina E. I., 2013, AJ, 145, 101
Kashikawa N., Misawa T., Minowa Y., Okoshi K., Hattori T., Toshikawa J., Ishikawa S., Onoue M., 2014, ApJ, 780, 116
Kauffmann G. et al., 2003, MNRAS, 341, 54
Kelvin L. S. et al., 2012, MNRAS, 421, 1007
Kennicutt R. C. J., 1998, ApJ, 498, 541
Kravtsov A. V., 2013, ApJ, 764, L31
Krogager J. K., Fynbo J. P. U., Møller P., Ledoux C., Noterdaeme P., Christensen L., Milvang-Jensen B., Sparre M., 2012, MNRAS, 424, L1
Krogager J. K., Møller P., Fynbo J. P. U., Noterdaeme P., 2017, MNRAS, 469, 2959
Kulkarni V. P., Hill J. M., Schneider G., Weymann R. J., Storrie-Lombardi L. J., Rieke M. J., Thompson R. I., Jannuzi B. T., 2000, ApJ, 536, 36
Kulkarni V. P., Hill J. M., Schneider G., Weymann R. J., Storrie-Lombardi L. J., Rieke M. J., Thompson R. I., Jannuzi B. T., 2001, ApJ, 551, 37
Kulkarni V. P., Fall S. M., Lauroesch J. T., York D. G., Welty D. E., Khare P., Truran J. W., 2005, ApJ, 618, 68
Kulkarni V. P., Khare P., Som D., Meiring J., York D. G., Péroux C., Lauroesch J. T., 2010, New Astron., 15, 735
Kulkarni V. P., Bowen D. V., Straka L. A., York D. G., Gupta N., Noterdaeme P., Srianand R., 2022, ApJ, 929, 150
Lan T.-W., Ménard B., Zhu G., 2014, ApJ, 795, 31
Ledoux C., Petitjean P., Fynbo J. P. U., Møller P., Srianand R., 2006, A&A, 457, 71
Lima-Dias C. et al., 2021, MNRAS, 500, 1323
Lofthouse E. K. et al., 2020, MNRAS, 491, 2057
Lofthouse E. K. et al., 2023, MNRAS, 518, 305
Lundgren B. F. et al., 2012, ApJ, 760, 49
Ly C., Malkan M. A., Rigby J. R., Nagao T., 2016, ApJ, 828, 67
Ma J., Brammer G., Ge J., Prochaska J. X., Lundgren B., 2018, ApJ, 857, L12
Marinacci F. et al., 2018, MNRAS, 480, 5113
McConnachie A. W., 2012, AJ, 144, 4
McKinney W. et al., 2010, in Proc. 9th Python in Science Conference. p. 51
Meiring J. D., Lauroesch J. T., Kulkarni V. P., Péroux C., Khare P., York D. G., Crotts A. P. S., 2007, MNRAS, 376, 557
Meiring J. D., Lauroesch J. T., Kulkarni V. P., Péroux C., Khare P., York D. G., 2009, MNRAS, 397, 2037
Ménard B., Chelouche D., 2009, MNRAS, 393, 808
Mowla L. A. et al., 2019, ApJ, 880, 57
Muzahid S., Kacprzak G. G., Charlton J. C., Churchill C. W., 2016, ApJ, 823, 66
Muzahid S. et al., 2020, MNRAS, 496, 1013
Nagamine K., Springel V., Hernquist L., 2004, MNRAS, 348, 435
Naiman J. P. et al., 2018, MNRAS, 477, 1206
Nelson D. et al., 2018, MNRAS, 475, 624
Nelson D. et al., 2019, Comput. Astrophys. Cosmol., 6, 2
Nielsen N. M., Churchill C. W., Kacprzak G. G., 2013, ApJ, 776, 115
Noterdaeme P. et al., 2012, A&A, 547, L1
Noterdaeme P., Petitjean P., Pâris I., Cai Z., Finley H., Ge J., Pieri M. M., York D. G., 2014, A&A, 566, A24
Peng C. Y., Ho L. C., Impey C. D., Rix H.-W., 2002, AJ, 124, 266
Péroux C., Howk J. C., 2020, ARA&A, 58, 363
Péroux C., Dessauges-Zavadsky M., D'Odorico S., Kim T.-S., McMahon R. G., 2003, MNRAS, 345, 480
Péroux C., Meiring J. D., Kulkarni V. P., Khare P., Lauroesch J. T., Vladilo G., York D. G., 2008, MNRAS, 386, 2209
Péroux C., Bouché N., Kulkarni V. P., York D. G., Vladilo G., 2011, MNRAS, 410, 2237
Péroux C., Bouché N., Kulkarni V. P., York D. G., Vladilo G., 2012, MNRAS, 419, 3060
Péroux C. et al., 2016, MNRAS, 457, 903
Péroux C. et al., 2019, MNRAS, 485, 1595
Péroux C. et al., 2022, MNRAS, 516, 5618
Pillepich A. et al., 2018, MNRAS, 475, 648
Prochaska J. X., Wolfe A. M., 2009, ApJ, 696, 1543
Prochaska J. X., Wolfe A. M., Howk J. C., Gawiser E., Burles S. M., Cooke J., 2007, ApJS, 171, 29
Rafelski M., Wolfe A. M., Chen H.-W., 2011, ApJ, 736, 48
Rafelski M., Wolfe A. M., Prochaska J. X., Neeleman M., Mendez A. J., 2012, ApJ, 755, 89
Rafelski M., Gardner J. P., Fumagalli M., Neeleman M., Teplitz H. I., Grogin N., Koekemoer A. M., Scarlata C., 2016, ApJ, 825, 87
Rahmani H. et al., 2016, MNRAS, 463, 980
Rahmani H. et al., 2018, MNRAS, 480, 5046

Rao S. M., Turnshek D. A., Nestor D. B., 2006, ApJ, 636, 610
Rhodin N. H. P., Christensen L., Møller P., Zafar T., Fynbo J. P. U., 2018, A&A, 618, A129
Rhodin N. H. P., Krogager J. K., Christensen L., Valentino F., Heintz K. E., Møller P., Zafar T., Fynbo J. P. U., 2021, MNRAS, 506, 546
Rubin K. H. R., Diamond-Stanic A. M., Coil A. L., Crighton N. H. M., Moustakas J., 2018, ApJ, 853, 95
Schroetter I. et al., 2016, ApJ, 833, 39
Schroetter I. et al., 2019, MNRAS, 490, 4368
Seo M., Ann H. B., 2022, MNRAS, 514, 5853
Shen S., Mo H. J., White S. D. M., Blanton M. R., Kauffmann G., Voges W., Brinkmann J., Csabai I., 2003, MNRAS, 343, 978
Som D., Kulkarni V. P., Meiring J., York D. G., Péroux C., Lauroesch J. T., Aller M. C., Khare P., 2015, ApJ, 806, 25
Springel V., White S. D. M., Tormen G., Kauffmann G., 2001, MNRAS, 328, 726
Springel V. et al., 2018, MNRAS, 475, 676
Sternberg A., Le Petit F., Roueff E., Le Bourlot J., 2014, ApJ, 790, 10
Straka L. A., Kulkarni V. P., York D. G., 2011, AJ, 141, 206
Tody D., 1986, in Crawford D. L.ed., Proc. SPIE Conf. Ser. Vol. 627, Instrumentation in Astronomy VI. SPIE, Bellingham, p. 733
Tumlinson J., Peeples M. S., Werk J. K., 2017, ARA&A, 55, 389
van der Wel A. et al., 2014, ApJ, 788, 28
Vladilo G., Abate C., Yin J., Cescutti G., Matteucci F., 2011, A&A, 530, A33
Weng S. et al., 2023, MNRAS, 519, 931
Wolfe A. M., Chen H.-W., 2006, ApJ, 652, 981
Wolfe A. M., Wills B. J., 1977, ApJ, 218, 39
Wolfe A. M., Gawiser E., Prochaska J. X., 2005, ARA&A, 43, 861
Wolfe A. M., Prochaska J. X., Jorgenson R. A., Rafelski M., 2008, ApJ, 681, 881
Wootten A., Thompson A. R., 2009, Proc. IEEE, 97, 1463
York D. G., Dopita M., Green R., Bechtold J., 1986, ApJ, 311, 610
Zabl J. et al., 2019, MNRAS, 485, 1961
Zafar T., Møller P., Péroux C., Quiret S., Fynbo J. P. U., Ledoux C., Deharveng J.-M., 2017, MNRAS, 465, 1613

SUPPORTING INFORMATION

Supplementary data are available at *MNRAS* online.

supp_data

Please note: Oxford University Press is not responsible for the content or functionality of any supporting materials supplied by the authors. Any queries (other than missing material) should be directed to the corresponding author for the article.

APPENDIX A: IMAGES OF INDIVIDUAL FIELDS

We show below the broad-band *HST* images in the reddest filter available for each of the remaining quasar fields, similar to the image of the field of Q0152+0023 shown in Fig. 1.

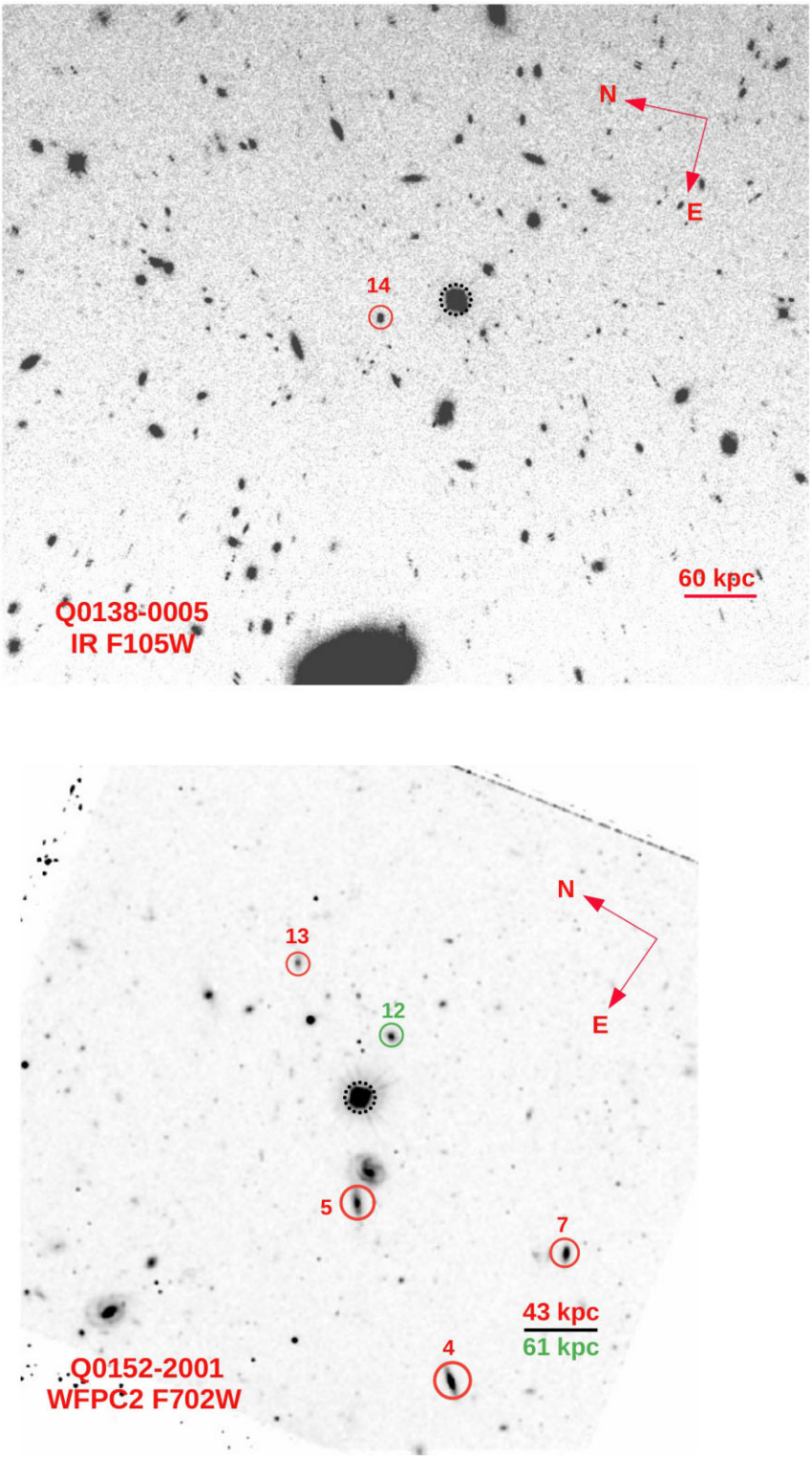

Figure A1. Similar figures to Fig. 1. Shown figures are the median-stacked images of the quasar fields in the full-frame. The solid circles represent the position of the associated galaxies in the field of view, while the dotted black circle denotes the QSO's position. The associated galaxies are located within ± 500 kms^{-1} of the absorber's redshift. The object identification number (ID) of these galaxies came from the MAH master table discussed in Péroux et al. (2022). While the scale bar corresponds to 60 kpc at $z_{\rm abs} = 0.7821$ for the top figure, the scale bar corresponds to 43 and 61 kpc at $z_{\rm abs} = 0.3830$ and 0.7802 for the bottom figure, respectively.

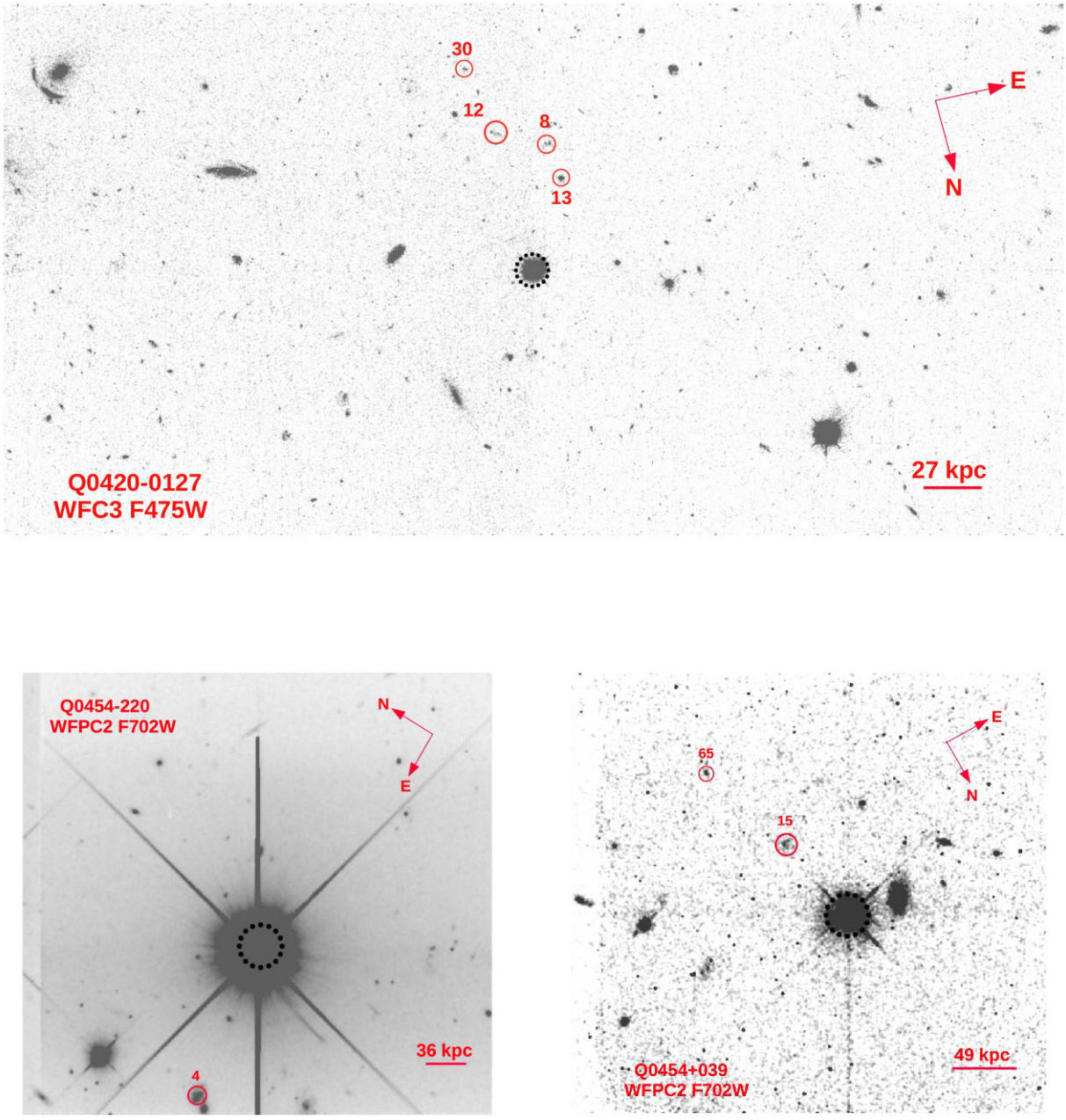

Figure A2. See Fig. A1 caption. The scale bar corresponds to 27 kpc at $z_{\rm abs} = 0.6331$ for the top figure, while in the bottom figures, the scale bar corresponds to 36 and 49 kpc at $z_{\rm abs} = 0.4833$ and 1.1532 for the left and right figures, respectively.

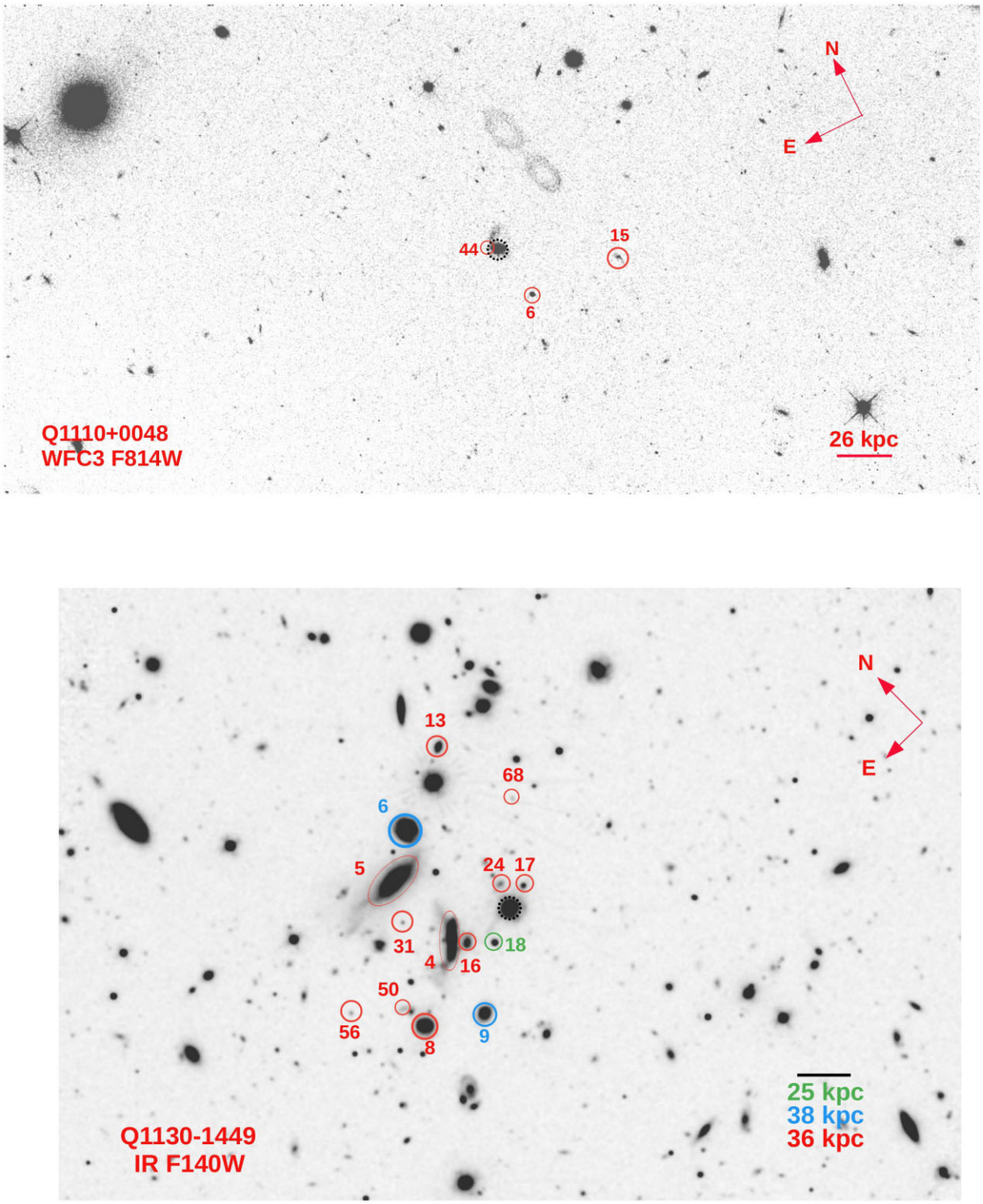

Figure A3. See Fig. A1 caption. The scale bar corresponds to 26 kpc at $z_{abs} = 0.5604$ for the top figure, while the scale bar corresponds to 25, 38, and 36 kpc at $z_{abs} = 0.1906$, 0.3283, and 0.3130 for the bottom figure, respectively.

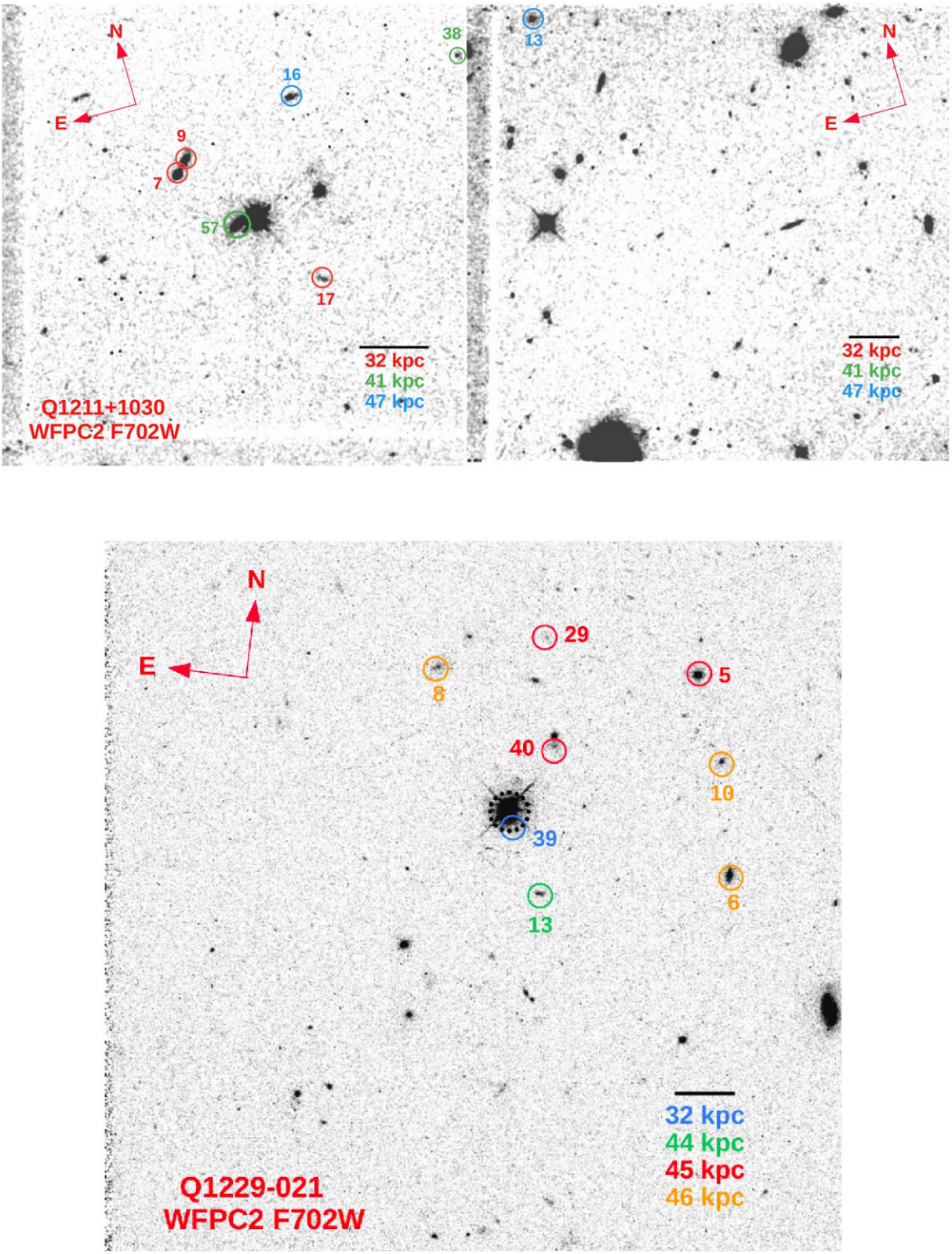

Figure A4. See Fig. A1 caption. The scale bar corresponds to 32, 41, and 47 kpc at $z_{abs} = 0.3929$, 0.6296, and 0.8999 for the top figures, while the scale bar corresponds to 32, 44, 45, and 46 kpc at $z_{abs} = 0.3950$, 0.7572, 0.7691, and 0.8311 for the bottom figure, respectively.

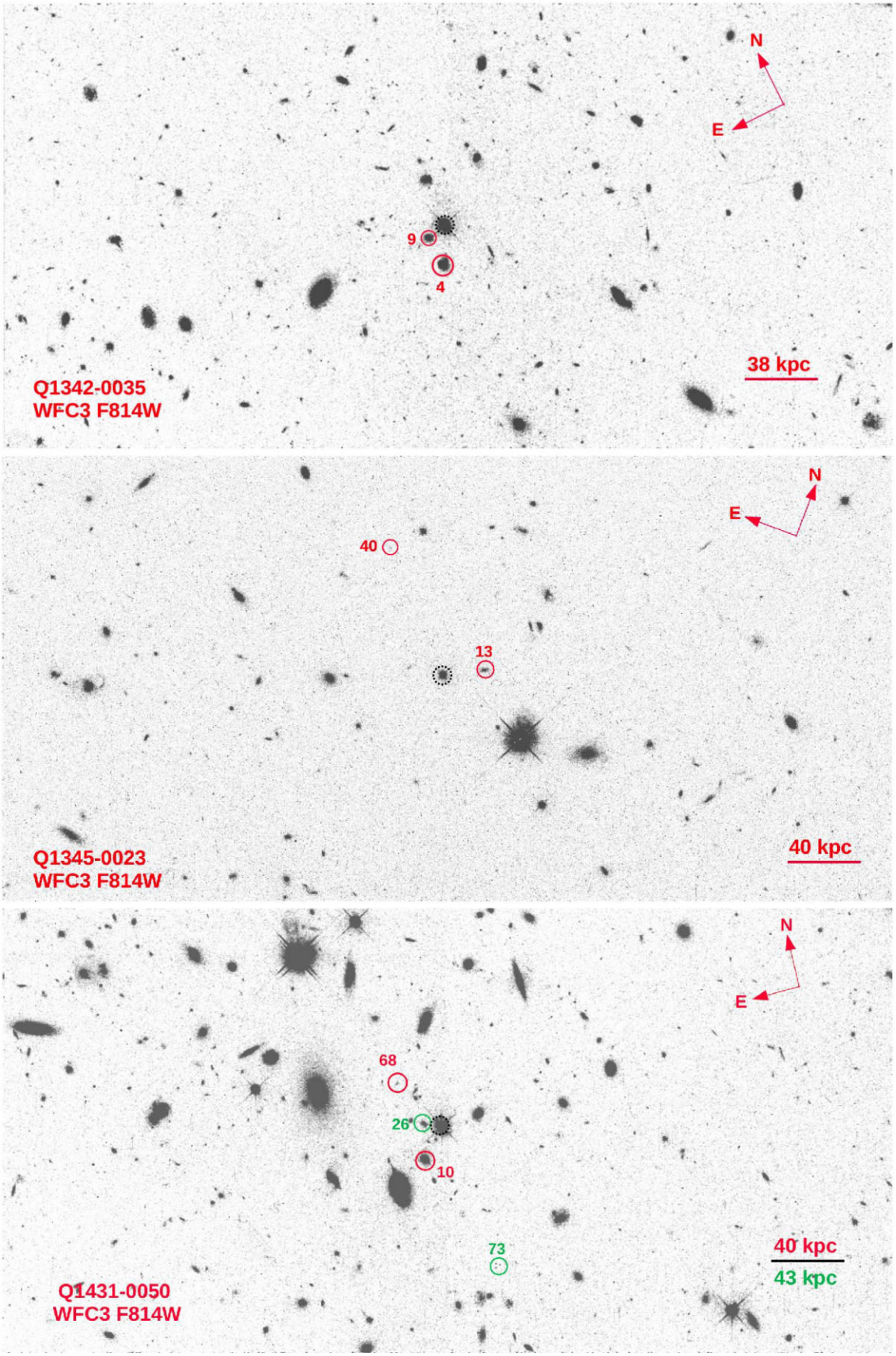

Figure A5. See Fig. A1 caption. The scale bar corresponds to 38 kpc at $z_{abs} = 0.5380$ for the top figure, 40 kpc at $z_{abs} = 0.6057$ for the middle figure, and 40 and 43 kpc at $z_{abs} = 0.6085$ and 0.6868 for the bottom figure, respectively.

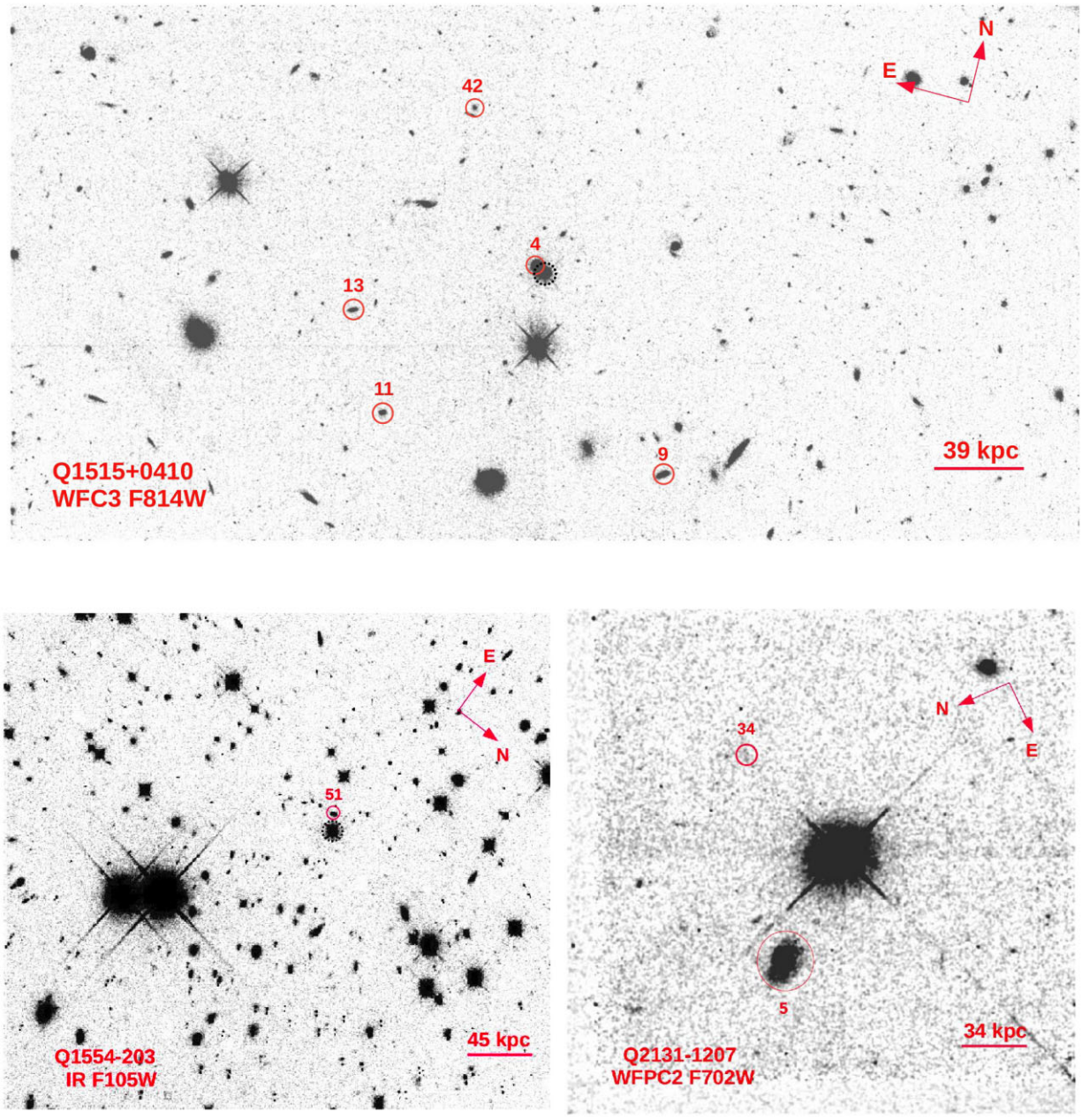

Figure A6. See Fig. A1 caption. The scale bar corresponds to 39 kpc at $z_{\rm abs} = 0.5592$ for the top figure, while in the bottom figures, the scale bar corresponds to 45 and 34 kpc at $z_{\rm abs} = 0.7869$ and 0.4298 for the left and right figures, respectively.

This paper has been typeset from a TEX/LATEX file prepared by the author.